
Supplementary information

**Photoelectrocatalytic biosynthesis fuelled
by microplastics**

In the format provided by the
authors and unedited

Photoelectrocatalytic biosynthesis fueled by microplastics

*Jinhyun Kim, Jinha Jang, Thomas Hilberath, Frank Hollmann, and Chan Beum Park**

Department of Materials Science and Engineering, Korea Advanced Institute of Science and Technology (KAIST), 291 Daehak-ro, Yuseong-gu, Daejeon 34141, Republic of Korea;
Department of Biotechnology, Delft University of Technology, Van der Maasweg 9, 2629 HZ Delft, The Netherlands.

*E-mail: parkcb@kaist.ac.kr

Table of Contents

Supplementary Methods

1. Chemicals and materials.
2. Bioelectrocatalytic (BEC) oxyfunctionalization reactions.
3. EC regeneration of NADH.
4. BEC amination and hydrogenation.
5. Fabrication and characterization of photoanodes.
6. PEC reformation of PET.
7. (Photo)electrochemical characterizations.
8. Quantification of H₂O₂, HO[•], and O₂.
9. Statistics.

Supplementary Tables

- Table 1:** Electrochemical impedance components of carbon fiber paper (CFP) and anthraquinone-2-carboxylic acid-anchored CFP (AQC/CFP).
- Table 2:** Decomposition rates of formate and acetate by Zr:α-Fe₂O₃.
- Table 3:** X-ray photoelectron spectroscopy (XPS) of Zr:α-Fe₂O₃ after PEC valorization of PET microplastics.
- Table 4:** Leakage of Zr:α-Fe₂O₃'s components into reaction solutions after PEC valorization of PET microplastics.
- Table 5:** Formate and acetate produced by Zr:α-Fe₂O₃|AQC/CFP- or Zr:α-Fe₂O₃|CFP-driven photobiosynthetic reactions.
- Table 6:** Gas chromatography oven programs for quantification of analytes.
- Table 7:** Traditional and emerging PEC systems.
- Table 8:** Comparison of biocatalytic BPEC, biocatalytic photocatalytic (BPC), and BEC approaches for enzymatic chemical synthesis.
- Table 9:** Synthetic performances of redox enzymes in state-of-the-art BPEC systems in a two-electrode configuration.
- Table 10:** Comparison of the production rates of formate and acetate through (photo)anodic PET reformation.

Supplementary Figures

- Figure 1.** Characterization of CFP.
- Figure 2.** Charge transfer resistances of CFP and AQC/CFP cathodes.
- Figure 3.** H₂O₂ production driven by AQC/CFP and CFP cathodes.

- Figure 4.** Pathway of O₂ reduction to H₂O₂.
- Figure 5.** Investigation of direct reduction of NAD⁺.
- Figure 6.** Spectroscopic analysis for NADH regeneration.
- Figure 7.** EC regeneration of NADH in different solvents.
- Figure 8.** Characterization of β-FeOOH and α-Fe₂O₃.
- Figure 9.** A series of control experiments for photoanodic reactions using PET microplastics.
- Figure 10.** Mechanistic studies of α-Fe₂O₃-driven photoanodic reactions.
- Figure 11.** PEC oxidation reactions of PET components and intermediates driven by α-Fe₂O₃ photoelectrode.
- Figure 12.** Effect of applied bias and PET concentration on PEC reformation of PET microplastics.
- Figure 13.** Characterization of Zr:α-Fe₂O₃ electrode synthesized using 2 mM Zr⁴⁺ ions.
- Figure 14.** Effect of Zr doping on PEC performance of hematite-based photoanodes.
- Figure 15.** Comparison of PEC properties of hematite-based photoanodes.
- Figure 16.** Analysis of charge recombination behaviors of hematite-based photoanodes.
- Figure 17.** Voltammetric analysis of Zr:α-Fe₂O₃ in the presence of formate or acetate.
- Figure 18.** Iteration test of Zr:α-Fe₂O₃-driven transformation of PET.
- Figure 19.** Changes in phase and chemical states of Zr:α-Fe₂O₃ photoanode after PEC reformation reactions.
- Figure 20.** Zr:α-Fe₂O₃'s PEC reformation of post-consumer PET items.
- Figure 21.** Controlled potential photoelectrolysis for enzymatic reactions.
- Figure 22.** Gas or liquid chromatograms of enzymatic products.
- Figure 23.** Effect of PET concentration on the rates of BPEC reactions.
- Figure 24.** Effect of applied bias on rAaeUPO-catalyzed hydroxylation reactions.
- Figure 25.** PEC properties used to augment enzymatic performances.

Supplementary Methods

Chemicals and materials. Poly(ethylene terephthalate), iron chloride hexahydrate, zirconium chloride, anthraquinone-2-carboxylic acid, formate, acetate, ethylene glycol, maleic acid, deuterium oxide, horseradish peroxidase, 2,2'-azino-bis(3-ethylbenzothiazoline-6-sulfonic acid), coumarin, L-glutamate dehydrogenase from liver bovine, (NH₄)₂SO₄, α -ketoglutaric acid, and 7-hydroxycoumarin (umbelliferone) were purchased from Sigma-Aldrich (St. Louis, MO, USA). Sodium hydroxide, potassium phosphate monobasic, and potassium phosphate dibasic were purchased from Samchun Chemicals (Seoul, Korea). All chemicals were used without further purification. We used type 1 ultrapure water (18 M Ω cm) from a Direct-Q[®] 5 UV ultrapure water purification system (Millipore Corp., USA). We synthesized a recombinant unspecific peroxygenase from *Agrocybe aegerita* (*rAaeUPO*) and an old yellow enzyme from *Thermus scotoductus* (*TsOYE*) according to the literature [*ACS Catal.* **9**, 7409-7417 (2019); *ACS Catal.* **9**, 10562-10566 (2019); *Sci. Adv.* **5**, eaax0501 (2019)]. We prepared denatured oxidoreductases by heating them at 363 K for 1 h.

Bioelectrocatalytic (BEC) oxyfunctionalization reactions. We applied AQC/CFP-driven H₂O₂ production to *rAaeUPO*-mediated oxyfunctionalization reactions in a one-compartment, three-electrode configuration. The electrolyte solution was O₂-rich potassium phosphate (KPi) buffer (100 mM, pH 6.0) containing 50 nM *rAaeUPO* and ethylbenzene. After the biocatalytic electrochemical reaction, we extracted oxyfunctionalized products using ethyl acetate, dried them over MgSO₄, and quantified them using a 7890A gas chromatograph (Agilent Technologies, USA) equipped with a flame ionization detector and a CP-Chirasil-Dex CB column (25 m \times 0.32 mm \times 0.25 μ m). We tabulated detailed oven temperature in **Supplementary Table 6**. The turnover frequency (TOF) of *rAaeUPO* was calculated using **Supplementary Equation 1**:

$$\text{TOF}_{rAaeUPO} \text{ (h}^{-1}\text{)} = \frac{\text{Concentration of enzymatic product}}{\text{Concentration of } rAaeUPO \times \text{Reaction time}} \quad (1)$$

EC regeneration of NADH. When we investigated the capability of CFP to reduce NAD⁺ to NADH, we immersed CFP electrode in sodium phosphate (NaPi) buffer (100 mM, pH 7.5) containing NAD⁺ and M_{ox} in three-electrode configuration [reference electrode: Ag/AgCl (3 M NaCl)]. We used a potentiostat/galvanostat (WMPG 1000, WonATech Co., Korea) to perform electrocatalytic analysis and controlled potential electrolysis. When we obtained linear sweep voltammograms and performed NADH regeneration tests, we added 0.25 mM M_{ox} and 1 mM NAD⁺ in O₂-depleted NaPi buffer. We quantified NADH using V-650 UV-Vis absorption spectrophotometer (Jasco Inc., Japan); NADH exhibits a characteristic peak at 340 nm and its molar extinction coefficient is reported to be 6220 M⁻¹ cm⁻¹ at 340 nm [*Angew. Chem. Int. Ed.* **57**, 13825-13828 (2018)]. Nuclear magnetic resonance spectroscopic (NMR) analysis was performed to prove the formation of 1,4-NADH. We used a 400 MHz AVANCE III HD Nanobay (Bruker Corp., USA) equipped with a tunable multinuclear probe (PA BBO 400S1 BBF-H-D-05 Z plus). We prepared a NMR sample (700 μ L) by diluting a reaction sample in a D₂O solvent (v/v, 9:1) containing sodium trimethylsilylpropanesulfonate (DSS)

(chemical shift standard). The NMR pulse sequence, relaxation delay, and temperature were zgesfpgp, 4 s, and 298 K, respectively.

BEC amination and hydrogenation. When we performed enzymatic amination reactions, 500 nM GDH, α -ketoglutarate, NH_4^+ , 0.25 mM M_{ox} , and 1 mM NAD^+ were dissolved in O_2 -depleted NaPi buffer (100 mM, pH 7.5). A controlled potential electrolysis was performed in a three-electrode configuration. The concentrations of α -ketoglutarate and L-glutamate were measured using a high-performance liquid chromatography (1260 Infinity liquid chromatography system, Agilent Technologies, USA) equipped with a variable wavelength detector and an Intersil C18 column. The eluent was phosphoric acid aqueous solution (0.05 wt%), a flow rate was 1.0 mL min^{-1} , and detection wavelength was 214 nm. When we drove enzymatic hydrogenation reactions, we added 5 μM *TsOYE*, 2-methyl-2-cyclohexen-1-one, CaCl_2 , NH_4^+ , 0.25 mM M_{ox} , and 1 mM NAD^+ in O_2 -depleted triethanolamine (TEOA)-buffered solution (100 mM, pH 7.5). The Ca^{2+} divalent ion is necessary for *TsOYE* catalysis. Because phosphate anions react with Ca^{2+} to form a precipitate, we replaced a phosphate buffer with a TEOA-buffered solution. This experiment was performed in a three-electrode configuration. The products of *TsOYE* were quantified using a 7890A gas chromatograph (Agilent Technologies, USA) equipped with a flame ionization detector and a CP-Chirasil-Dex CB column ($25 \text{ m} \times 0.32 \text{ mm} \times 0.25 \mu\text{m}$). We tabulated detailed oven temperature in **Supplementary Table 6**. The TOFs of GDH and *TsOYE* were calculated using **Supplementary Equations 2 and 3**:

$$\text{TOF}_{\text{GDH}} (\text{h}^{-1}) = \frac{\text{Concentration of enzymatic product}}{\text{Concentration of GDH} \times \text{Reaction time}} \quad (2)$$

$$\text{TOF}_{\text{TsOYE}} (\text{h}^{-1}) = \frac{\text{Concentration of enzymatic product}}{\text{Concentration of TsOYE} \times \text{Reaction time}} \quad (3)$$

Fabrication and characterization of photoanodes. We synthesized a hematite photoanode via solution-based processing and high temperature annealing. A commercial fluorine-doped tin oxide glass (F:SnO₂, TEC-7, Pilkington) was rinsed with acetone, isopropyl alcohol, and deionized water. To deposit a β -FeOOH nanostructure on the F:SnO₂ substrate, we prepared a precursor solution containing 150 mM FeCl₃·6H₂O and 1 M NaNO₃ in deionized water. The substrate was immersed in the solution and heated in a Lindberg/Blue M muffle furnace (Fisher Scientific Co., USA) at 100 °C for 6 h. To transform β -FeOOH into α -Fe₂O₃, the electrode was annealed at 800 °C for 20 min. When we prepared a Zr: α -Fe₂O₃, we added ZrCl₄ (0 to 2.5 mM) into the precursor solution, and followed the aforementioned method. The morphology of an electrode was examined using an S-4800 field emission scanning electron microscope (Hitachi High-Tech Corp., Japan) or a Quattro S environmental scanning electron microscope (ThermoFisher Scientific Inc., USA). The crystallinities of akaganeite and hematite films were investigated using a SmarLab (Rigaku Co., Japan) with a scan rate of 4° min^{-1} and a Cu K α radiation wavelength of 1.5406 Å. We used K-Alpha X-ray photoelectron spectrometer (ThermoFisher Scientific Inc., USA) to investigate chemical states of the photoanodes. Ultraviolet photoelectron spectra were recorded using AXIS

Supra⁺ (Kratos Analytical Ltd., Japan) with a photon energy of 21.2 eV (He I radiation). We estimated a work function (W) using **Supplementary Equation 4**:

$$W = -h\nu + E_{\text{cutoff,high}} - E_{\text{F}} \quad (4)$$

where $h\nu$ is the energy of incident light (21.2 eV), $E_{\text{cutoff,high}}$ is the high-binding-energy cutoff, and E_{F} is the Fermi level. A valence band edge potential (E_{VB}) was calculated according to **Supplementary Equation 5**:

$$E_{\text{VB}} = W - (E_{\text{cutoff,low}} - E_{\text{F}}) \quad (5)$$

where $E_{\text{cutoff,low}}$ is the low-binding-energy cutoff. The unit conversion from eV (vs. vacuum) to V_{RHE} is in accordance with **Supplementary Equation 6**:

$$E_{\text{eV}} = (-e) \times (E_{\text{RHE}} + 4.5 \text{ V}) \quad (6)$$

where E_{eV} is the energy in the unit of eV (vs. vacuum), E_{RHE} is the potential in the unit of V_{RHE} , and e is the elementary charge.

PEC reformation of PET. PEC reformation of PET was performed in a three-electrode configuration. The configuration consisted of working electrode (1.7 cm²), Hg/HgO (1 M NaOH) reference electrode, and Pt counter electrode. Compared to Ag/AgCl reference electrode, Hg/HgO reference electrode is more appropriate for long-term PEC reactions under alkaline conditions. When the molarity of OH⁻ ions is higher than 0.1 M, OH⁻ ions react with Ag⁺ ions in the Ag/AgCl reference electrode to form AgOH and Ag₂O, which (i) impairs the AgCl coating of the RE, (ii) changes the RE's potential, and (iii) damages frit pores of the Ag/AgCl. When we performed controlled potential photoelectrolysis, (i) the electrolyte volume was 2.0 mL unless otherwise specified, (ii) the light source was a xenon lamp (Newport Co., USA), and (iii) an electrical bias was provided using potentiostat/galvanostat (WMPG 1000, WonATech Co., Korea). All potentials have been quoted versus reversible hydrogen electrode (RHE) according to the following equation (**Supplementary Equation 7**)

$$E_{\text{RHE}} (\text{V}) = E_{\text{Hg/HgO}} (\text{V}) + 0.140 + (0.059 \times \text{pH}) \quad (7)$$

When we investigated which species (e.g., h⁺, H₂O₂, HO[•]) performed the waste-to-chemical conversion, we added Na₂SO₃ (hole scavenger), sodium pyruvate (H₂O₂ scavenger), or *tert*-butyl alcohol (HO[•] scavenger) into unpretreated PET solution (1 mg mL⁻¹ PET microplastics, 5 M NaOH). When we tested the effect of O₂ on the PET reformation reaction, we purged N₂ gas into the anodic electrolyte solution before and during photoelectrochemical (PEC) reaction. We used 6-cm² Zr:α-Fe₂O₃ photoanode during investigation of long-term PEC reactions using post-consumer PET items.

(Photo)electrochemical characterizations. We performed linear sweep voltammetric analysis and controlled potential photoelectrolysis using potentiostat/galvanostat (WMPG 1000, WonATech Co., Korea) and xenon arc lamp (Newport Co., USA). We estimated J_{abs} (photocurrent density obtained when absorbed photon-to-current conversion efficiency is

100%), η_{bulk} (charge transfer efficiency in the bulk), and η_{surface} (charge transfer efficiency at the semiconductor|electrolyte interface). The light absorption by a photocatalyst generates photocurrent density (J), the magnitude of which decreases by two major losses (i.e., charge recombination in the bulk and at the surface of the photocatalyst). Thus, the photocurrent density from substrate oxidation (J_{sub}) can be expressed according to **Supplementary Equation 8**

$$J_{\text{sub}} = J_{\text{abs}} \times \eta_{\text{bulk}} \times \eta_{\text{surface}} \quad (8)$$

The estimation of η_{bulk} requires the photocurrent density from sulfite oxidation (J_{SO_3}) because sulfite oxidation is so rapid to suppress the surface recombination of charge carriers, making η_{surface} be almost 1. Thus, the **Supplementary Equation 8** becomes **Supplementary Equations 9 and 10**

$$J_{\text{SO}_3} = J_{\text{abs}} \times \eta_{\text{bulk}} \quad (9)$$

$$\eta_{\text{bulk}} = J_{\text{SO}_3} \times J_{\text{abs}}^{-1} \quad (10)$$

From **Supplementary Equations 8 and 9**, the estimation of η_{surface} is **Supplementary Equation 11**

$$\eta_{\text{surface}} = J_{\text{sub}} \times J_{\text{SO}_3}^{-1} \quad (11)$$

J_{abs} (mA cm^{-2}) is estimated according to **Supplementary Equation 12**

$$J_{\text{abs}} = \int_a^b \frac{\lambda}{1240} \times P_0(\lambda) \times (1 - 10^{-A(\lambda)}) d\lambda \quad (12)$$

where λ is the wavelength of incident light (nm), $P_0(\lambda)$ is the corresponding power density ($\text{mW cm}^{-2} \text{ nm}^{-1}$) provided by a solar simulator (AM 1.5G), and $A(\lambda)$ is the absorbance of the photocatalyst [*Adv. Mater.* **31**, 1806938 (2019)]. To estimate J_{SO_3} and J_{PET} , we used 300 mM Na_2SO_3 solution and pretreated PET solution, respectively. We acquired a Mott-Schottky plot using impedance analyzer (ZIVE SP1, WonATech Co., Korea) at 1 kHz under dark conditions. From the plot, we measured the capacitance (C) of the space-charge region at the Fe_2O_3 |electrolyte interface using the following equation (**Supplementary Equation 13**):

$$\frac{1}{C^2} = \frac{2}{\epsilon\epsilon_0 A^2 e N_D} \left(V - V_{\text{fb}} - \frac{kT}{e} \right) \quad (13)$$

where ϵ is the dielectric constant of Fe_2O_3 (80), ϵ_0 is the permittivity in vacuum ($8.854 \times 10^{-12} \text{ C V}^{-1} \text{ m}^{-1}$), A is the area (m^2) of the photoelectrode, e is the elementary charge ($1.602 \times 10^{-19} \text{ C}$), N_D is the free carrier density (m^{-3}), V is the applied potential, V_{fb} is the flat band potential of the photoelectrode, k is Boltzmann constant ($8.617 \times 10^{-5} \text{ eV K}^{-1}$), and T is the absolute temperature (K). Furthermore, we obtained a Nyquist plot using the same impedance analyzer (ZIVE SP1, WonATech Co., Korea) at a frequency of 100,000 to 0.1 Hz and an AC potential amplitude of 10 mV. We fitted the Nyquist plot to calculate a charge-transfer resistance using a Zman software (WonATech Co., Korea).

Quantification of H₂O₂, HO[•], and O₂. We determined the amount of H₂O₂ spectrophotometrically using ABTS assay. We used coumarin assay to detect hydroxyl radicals (HO[•]) [*Appl. Catal., B* **81**, 295-302 (2008)]. We added 1 mM coumarin in electrolyte solution and drove a PEC reaction. After the reaction, we monitored a change in fluorescence intensity at 455 nm ($\lambda_{\text{ex}} = 332$ nm) to detect 7-hydroxycoumarin (7-HC). Note that a coumarin reacts with two HO[•] to form a 7-HC. We detected O₂ gas using micro gas chromatograph (Micro GC fusion, INFICON Inc., USA) equipped with a Molsieve 5A column and a micro thermal conductivity detector.

Statistics. For a sample with n observations x_i , the measurements are given as the unweighted mean (\bar{x}) \pm standard deviation (σ). Unweighted means and standard deviations were calculated as follows (**Supplementary Equations 14 and 15**):

$$\bar{x} = \sum_{i=1}^n \frac{x_i}{n} \quad (14)$$

$$\sigma = \sqrt{\sum_{i=1}^n \frac{(x_i - \bar{x})^2}{n-1}} \quad (15)$$

We used one-way analysis of variance (ANOVA) to investigate statistically significant differences between groups. We used Microsoft Excel software to estimate p -values in ANOVA. The number of samples in a group and the significance level were three ($n = 3$) and 0.05, respectively, unless otherwise stated.

Supplementary Tables

Supplementary Table 1. Electrochemical impedance components of carbon fiber paper (CFP) and anthraquinone-2-carboxylic acid-anchored CFP (AQC/CFP).

Sample	R_s (Ω)	R_{ct} ($k\Omega$)	CPE (μF)
CFP	28.90	0.99	85.89
AQC/CFP	37.76	0.38	86.10

We estimated these components by fitting a Nyquist plot to an equivalent circuit model, which consists of a solution resistance (R_s), a charge-transfer resistance (R_{ct}), and a constant phase element (CPE). We purged O_2 gas into an electrolyte for at least 40 min prior to the impedance experiments.

Supplementary Table 2. Decomposition rates of formate and acetate by Zr: α - Fe_2O_3 .

Light	Applied bias (V_{RHE})	Formate decomposition rate ($mM h^{-1}$)	Acetate decomposition rate ($mM h^{-1}$)
Solar light (1 sun)	0.8	ND	ND
	0.9	ND	ND
	1.0	ND	ND
	1.1	ND	ND
	1.2	ND	ND

Reaction condition: 1.7-cm^2 Zr: α - Fe_2O_3 , formate or acetate (1 mM), 5 M NaOH, simulated solar light (1 sun), applied bias, and 303 K. ND: not detected. Formate and acetate were quantified using quantitative 1H NMR analysis.

Supplementary Table 3. X-ray photoelectron spectroscopy (XPS) of Zr: α -Fe₂O₃ after PEC valorization of PET microplastics.

Cycle number	Fe 2p		Zr 3d	
	Position of p _{1/2} (eV)	Position of p _{3/2} (eV)	Position of d _{3/2} (eV)	Position of d _{5/2} (eV)
0	724.5	711.0	184.5	182.2
1	724.3	711.0	184.5	182.2
2	724.5	711.0	184.6	182.2
3	724.4	711.2	184.5	182.2
4	724.3	711.0	184.5	182.3
5	724.3	711.0	184.6	182.3
6	724.4	710.8	184.5	182.2
7	724.5	711.1	184.6	182.2

Reaction condition: 1.7-cm² Zr: α -Fe₂O₃, pretreated PET solution (5 mg mL⁻¹ PET microplastics, 5 M NaOH), simulated solar light (1 sun), 1.1 V_{RHE}, and 303 K.

Supplementary Table 4. Leakage of Zr: α -Fe₂O₃'s components into reaction solutions after PEC valorization of PET microplastics.

Number of repetition	Zr concentration (mg L ⁻¹)	Fe concentration (mg L ⁻¹)
0	ND	ND
1	ND	ND
2	ND	ND
3	ND	ND
4	ND	ND
5	ND	ND
6	ND	ND
7	ND	ND

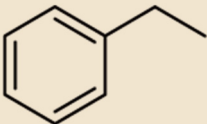
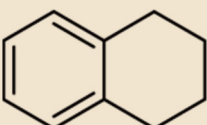
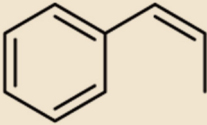
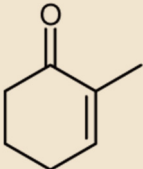
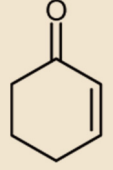
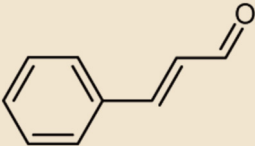
Reaction condition: 1.7-cm² Zr: α -Fe₂O₃, pretreated PET solution (5 mg mL⁻¹ PET microplastics, 5 M NaOH), simulated solar light (1 sun), 1.1 V_{RHE}, and 303 K. When a cycle of the PEC experiment was complete, we washed Zr: α -Fe₂O₃'s surface using deionized water, immersed it into a new reaction solution, and drove the PET valorization reaction again. ND: not detected.

Supplementary Table 5. Formate and acetate produced by Zr: α -Fe₂O₃|AQC/CFP- or Zr: α -Fe₂O₃|CFP-driven photobiosynthetic reactions.

Cathodic site	Photoanodic site ^[a]	
	Formate (μmol) ^[b]	Acetate (μmol) ^[b]
<i>rAae</i> UPO-driven hydroxylation of ethylbenzene	5.47	0.55
GDH-driven amination of α -ketoglutarate	68.61	6.99
<i>TsOYE</i> -driven hydrogenation of 2-methyl-2-cyclohexen-1-one	4.55	0.57

^[a]Electrolyte solution: pretreated PET solution (50 mg mL⁻¹ Starbucks PET microplastics, 5 M NaOH). Light intensity: 1 sun. ^[b]Products were quantified using quantitative NMR spectroscopy.

Supplementary Table 6. Gas chromatography oven programs for quantification of analytes.

Substrate	Temperature profile	Retention time (min) ^[a]
	90 °C for 5 min, 20 °C min ⁻¹ to 110 °C and hold for 13.5 min, 40 °C min ⁻¹ to 180 °C and hold for 1.5 min	Ethylbenzene: 4.4 (<i>R</i>)-1-Phenylethanol: 16.4 (<i>S</i>)-1-Phenylethanol: 17.3 1-Octanol: 11.4
	90 °C for 1 min, 5 °C min ⁻¹ to 140 °C and hold for 10 min, 80 °C min ⁻¹ to 180 °C and hold for 1 min	1,2,3,4-Tetrahydronaphthalene: 9.4 (<i>R</i>)-1,2,3,4-Tetrahydro-1-naphthol: 20.9 (<i>S</i>)-1,2,3,4-Tetrahydro-1-naphthol: 20.5 1-Octanol: 8.6
	90 °C for 5 min, 20 °C min ⁻¹ to 110 °C and hold for 5 min, 40 °C min ⁻¹ to 150 °C and hold for 3 min	Cyclohexane: 3.2 Cyclohexanol: 8.3 1-Octanol: 11.3
	90 °C for 2 min, 10 °C min ⁻¹ to 140 °C and hold for 5 min, 20 °C min ⁻¹ to 180 °C and hold for 3 min	<i>cis</i> -β-Methylstyrene: 5.4 (1 <i>R</i> ,2 <i>S</i>)-1-Phenylpropylene oxide: 7.7 (1 <i>S</i> ,2 <i>S</i>)-1-Phenylpropylene oxide: 7.3
	90 °C for 2 min, 4 °C min ⁻¹ to 115 °C, 20 °C min ⁻¹ to 180 °C and hold for 2 min	2-Methyl-2-cyclohexen-1-one: 7.1 (<i>R</i>)-2-Methylcyclohexanone: 6.4 (<i>S</i>)-2-Methylcyclohexanone: 6.3 1-Octanol: 9.5
	90 °C for 2 min, 5 °C min ⁻¹ to 180 °C and hold for 4 min	2-Cyclohexen-1-one: 6.1 Cyclohexanone: 5.5 1-Octanol: 9.2
	90 °C for 2 min, 20 °C min ⁻¹ to 115 °C, 10 °C min ⁻¹ to 200 °C and hold for 1 min	<i>trans</i> -3-Phenyl-2-propenal: 8.9 3-Phenylpropionaldehyde: 7.4 1-Octanol: 6.5

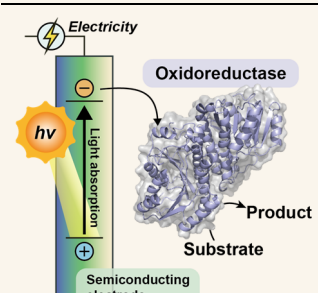
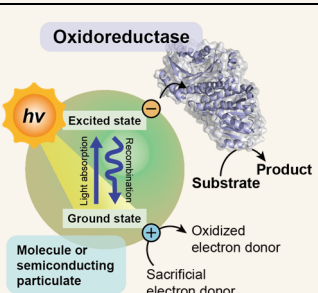
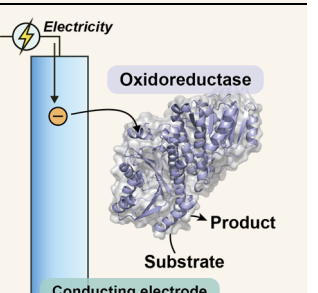
^[a]1-Octanol was used as an internal standard.

Supplementary Table 7. Traditional and emerging PEC systems.

PEC system	Scheme	Product
Traditional PEC cells		
Regenerative cells ^[a]		Electricity
Photosynthetic cells ^[a]		Fuels (e.g., H ₂)
Emerging field of PEC platforms to develop new concepts for solar energy conversion		
Biocatalytic PEC systems ^[b]	<ul style="list-style-type: none"> • Synthetically useful reactions • Excellent catalytic efficiencies • Excellent chemo-, regio- and stereoselectivities • Benign conditions 	Enzymatic products

^[a]*Nature* **414**, 338-344 (2001). ^[b]*Curr. Opin. Chem. Biol.* **49**, 122-129 (2019). CB: conduction band. VB: valence band. GDH: L-glutamate dehydrogenase. OYE: old yellow enzyme. FDH: formate dehydrogenase. UPO: unspecific peroxxygenase. EWG: electron-withdrawing group.

Supplementary Table 8. Comparison of biocatalytic BPEC, biocatalytic photocatalytic (BPC), and BEC approaches for enzymatic chemical synthesis.

	BPEC	BPC	BEC
Platform			
Energy source	Light and electricity	Light	Electricity
Abiotic catalyst	<ul style="list-style-type: none"> Semiconducting electrode (e.g., α-Fe₂O₃, BiVO₄^[a]) Conducting electrode (e.g., carbon fiber paper, carbon nanotube film^[a]) 	<ul style="list-style-type: none"> Molecule (e.g., flavin^[b], solvatochromic dye^[c]) Semiconducting particulate (e.g., graphitic C₃N₄^[d], carbon nanodot^[e]) 	<ul style="list-style-type: none"> Conducting electrode (e.g., gold-based electrode^[f], tin oxide electrode^[f], carbon-based electrode^[g])
Photoexcited charge carriers' recombination	Suppressed ^[h]	Generally severe ^[h]	Not applicable
Protection of enzymes from oxidation	Possible ^[h,i]	Impossible	Possible ^[h,i]
Mass-transfer limitations	Likely ^[j]	Unlikely ^[k]	Likely ^[j]
Amount of electrical bias	Lower than BEC systems	Not applicable	Higher than BPEC systems

^[a]Nat. Commun. **9**, 4208 (2018). ^[b]ChemSusChem **14**, 3054-3058 (2021); ACS Catal. **9**, 4115-4144 (2019). ^[c]ACS Appl. Energy Mater. **3**, 1215-1221 (2020). ^[d]Biomacromolecules **18**, 3551-3556 (2017). ^[e]Angew. Chem. Int. Ed. **57**, 13825-13828 (2018). ^[f]ChemCatChem **2**, 762-782 (2010). ^[g]Chem. Rev. **120**, 12903-12993 (2020). ^[h]Angew. Chem. Int. Ed. **57**, 7958-7985 (2018); Curr. Opin. Chem. Biol. **49**, 122-129 (2019). ^[i]Using spatial separation of anodic and cathodic sites. ^[j]Catalytic reactions occur at the electrode|electrolyte interface. ^[k]If all catalysts and reactants are homogeneously distributed in reaction medium.

Supplementary Table 9. Synthetic performances of redox enzymes in state-of-the-art BPEC systems in a two-electrode configuration.

BPEC systems	Redox enzyme	TTN _{rAaeUPO}	e.e. (%)	
FeOOH/BiVO ₄ CIGS CN/rGO ^[a]		43,000 ^[c]	>99	
Mo:BiVO ₄ IO-ITO ^[b]	rAaeUPO	10,000 ^[c]	>99	
Zr:α-Fe ₂ O ₃ AQC/CFP (This work)		362,000	>99	
BPEC systems	Redox enzyme	TTN _{GDH}	TTN _{M_{ox}} ^[e]	TTN _{NAD⁺} ^[f]
FeOOH/BiVO ₄ Perovskite CNT ^[d]		108,000	100 ^[c]	25 ^[c]
Zr:α-Fe ₂ O ₃ CFP (This work)	GDH	144,000	290	72
BPEC systems	Redox enzyme	TTN _{TsOYE}	e.e. (%)	
FeOOH/BiVO ₄ CNT/p-g-C ₃ N ₄ ^[e]		250 ^[c]	84 ^[c]	
Mo:BiVO ₄ IO-ITO ^[b]	TsOYE	110 ^[c]	82	
Zr:α-Fe ₂ O ₃ CFP (This work)		1,300	>99	

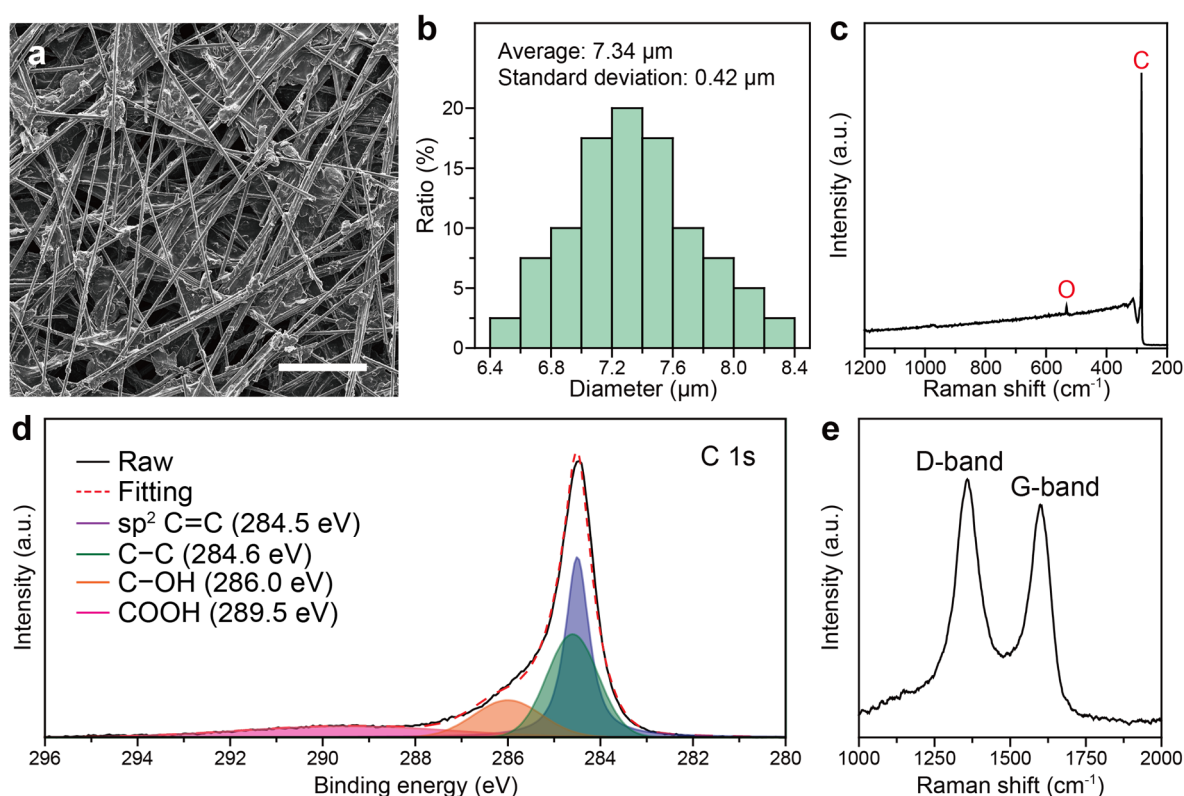
^[a]*ACS Catal.* **9**, 10562-10566 (2019). ^[b]*Angew. Chem. Int. Ed.* **59**, 15886-15890 (2020). ^[c]Approximate estimation based on data provided by the corresponding reference. ^[d]*Nat. Commun.* **9**, 4208 (2018). ^[e]*Adv. Funct. Mater.* **28**, 1705232 (2018). ^[e]TTN_{M_{ox}} = [Maximum product concentration during enzymatic reaction] × [Concentration of M_{ox}]⁻¹. ^[f]TTN_{NAD⁺} = [Maximum product concentration during enzymatic reaction] × [Concentration of NAD⁺]⁻¹. e.e.: enantiomeric excess.

Supplementary Table 10. Comparison of the production rates of formate and acetate through (photo)anodic PET reformation.

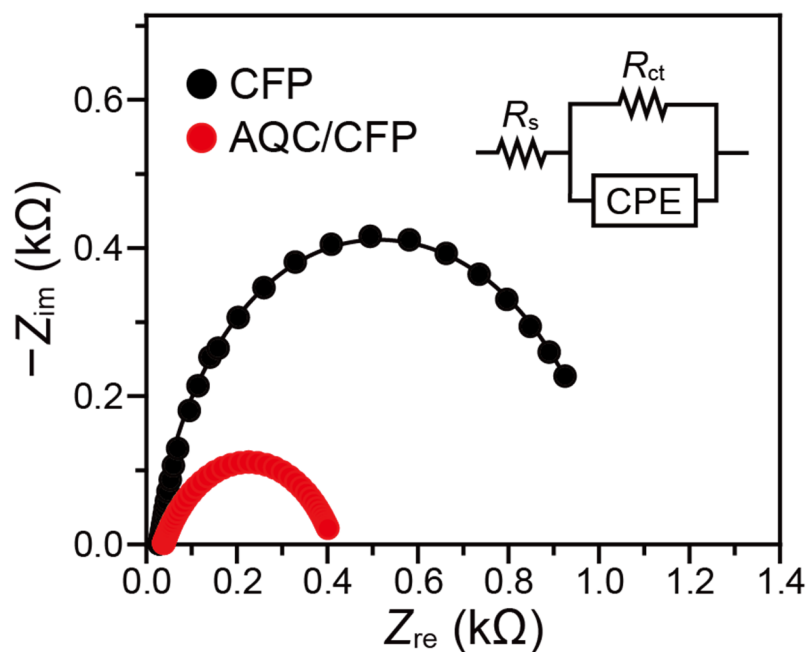
(Photo)anode	Light	Electrical bias (V _{RHE})	Production rate ($\mu\text{mol cm}_{\text{anode}}^{-2} \text{h}^{-1} \text{g}_{\text{PET}}^{-1}$)	
			Formate	Acetate
Nickel-phosphorous alloy nanoparticulate thin film ^[a]	NA	1.5	59.7 ^[b]	No information
Zr: α -Fe ₂ O ₃ (This work)	Solar light (1 sun)	1.1	94.1	3.1

^[a]*Appl. Catal. B-Environ.* **296**, 120351 (2021). ^[b]Approximate estimation based on data provided by the corresponding reference. NA: not applicable.

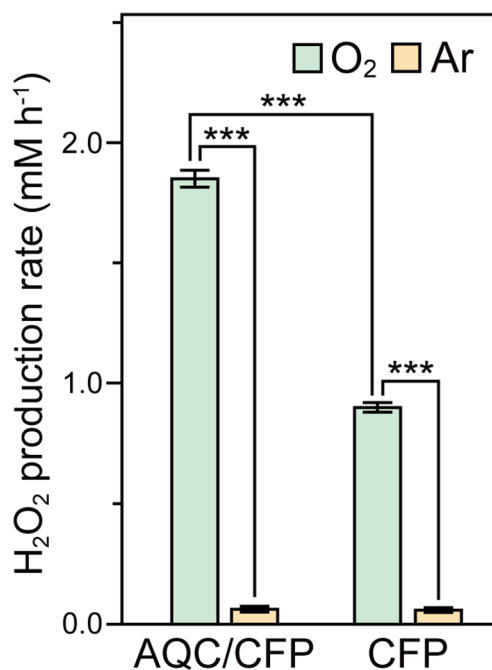
Supplementary Figures



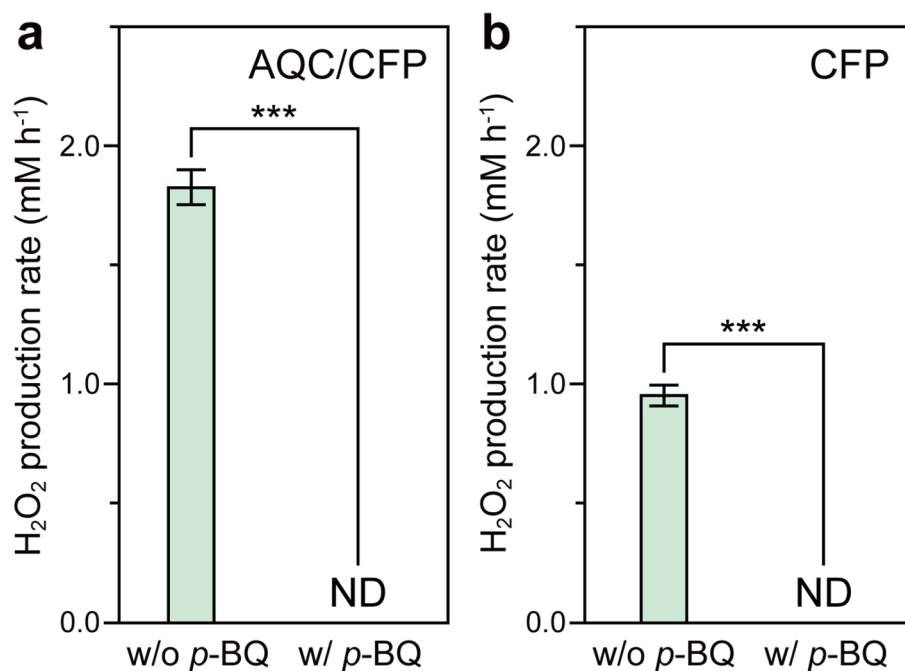
Supplementary Figure 1. Characterization of CFP. (a) Plan-view scanning electron microscopic (SEM) image of CFP. Scale bar: 0.2 mm. (b) Histogram of diameters of carbon fibers in CFP. (c) XPS survey scan of CFP. (d) C 1s XPS of CFP. Literature about binding energy positions: *Adv. Funct. Mater.* **28**, 1705232 (2018); *J. Phys. Chem. Lett.* **2**, 1556-1562 (2011); *Appl. Surf. Sci.* **167**, 99-106 (2000). (e) Raman spectrum of CFP. The intensity ratio of D-band to G-band (I_D/I_G) was 1.11. According to our scanning electron microscopic image in **panel (a)**, the CFP consisted of randomly oriented microfibers [diameter: $7.34 \pm 0.42 \mu\text{m}$, **panel (b)**] and some agglomerates. From XPS analysis, we detected CFP's C and O atoms (atomic ratio, 98:2) and multiple carbon-based functional groups (e.g., conjugated C=C, C-C, C-OH, and COOH) [**panels (c) and (d)**]; consistent with the spectroscopic result, CFP's Raman spectrum shows a D-band and G-band [**panel (e)**], which we attribute to structural defects (e.g., C-C, C-OH, COOH) and graphite structure's sp^2 -hybridized C-C bonds, respectively [*ACS Appl. Energy Mater.* **2**, 2324-2336 (2019); *Chem. Soc. Rev.* **47**, 1822-1873 (2018)].



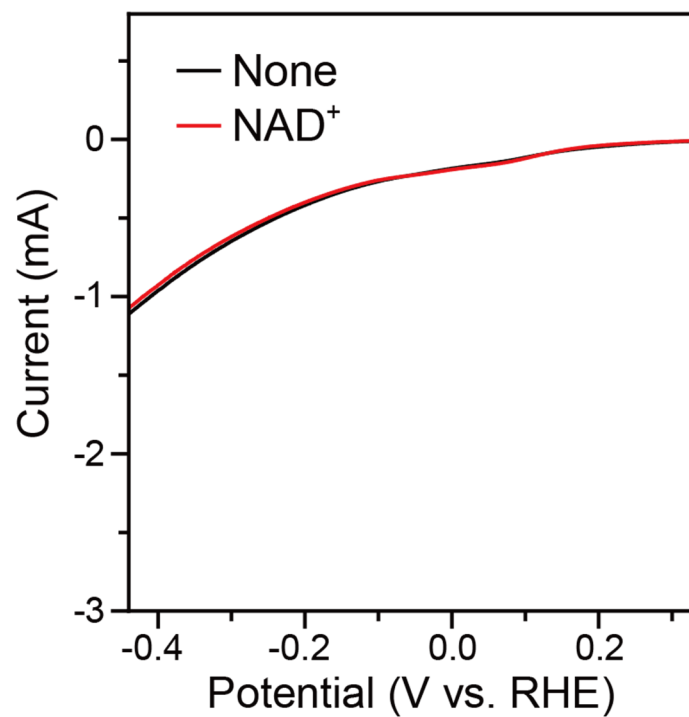
Supplementary Figure 2. Charge transfer resistances of CFP and AQC/CFP cathodes. Nyquist plots of CFP and AQC/CFP electrodes at 0.16 V_{RHE} in KPi buffer (100 mM, pH 6.0). The buffer was purged with O₂ gas at least for 40 min before electrochemical experiments. We estimated charge-transfer resistances by fitting their Nyquist plots to an equivalent circuit model (inset) that consists of a solution resistance (R_s), a charge-transfer resistance (R_{ct}), and a constant phase element (CPE).



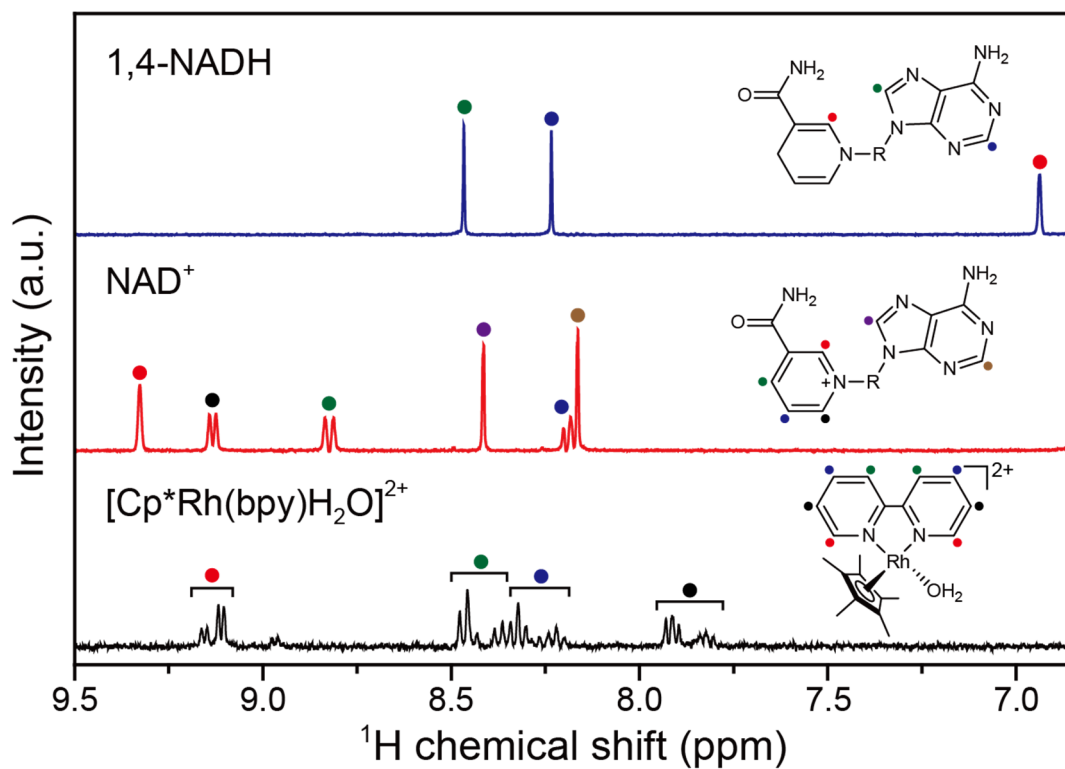
Supplementary Figure 3. H₂O₂ production driven by AQC/CFP and CFP cathodes. Electrolyte solution: KPi buffer (100 mM, pH 6.0). Applied bias: 0.16 V_{RHE}. Error bar: standard deviation ($n = 3$). Geometrical surface areas of the cathodes: 1 cm². We performed statistical analysis using one-way ANOVA ($n = 3$, ***: $p < 0.001$).



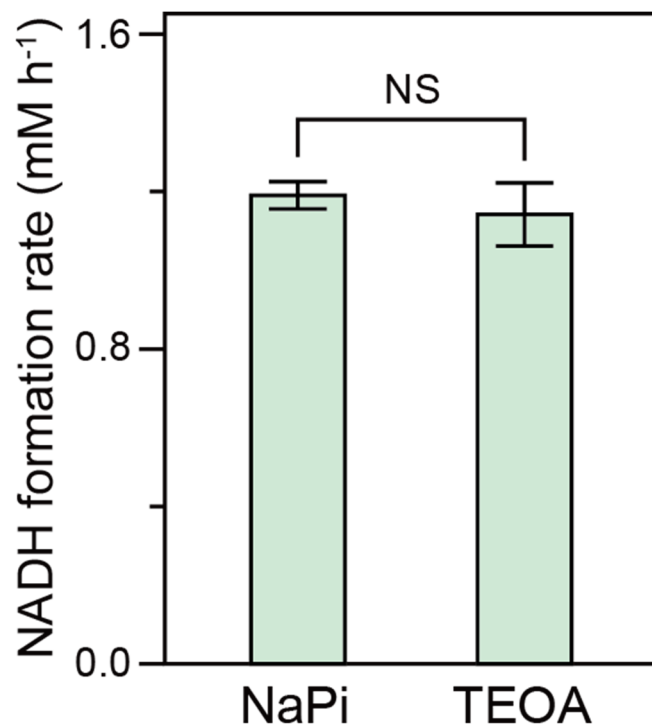
Supplementary Figure 4. Pathway of O₂ reduction to H₂O₂. Effect of *p*-benzoquinone (*p*-BQ) on the electrocatalytic production of H₂O₂ driven by (a) AQC/CFP and (b) CFP. Geometrical surface areas of the cathodes: 1 cm². Electrolyte solution: O₂-rich KPi buffer (100 mM, pH 6.0). Concentration of *p*-BQ: 10 mM. Applied bias: 0.1 V_{RHE}. ND: not detected. Error bar: standard deviation ($n = 3$). One-way ANOVA ($n = 3$, ***: $p < 0.001$). We investigated the pathway of O₂ reduction to H₂O₂. The reduction reaction can occur via (i) a two-step, single-electron reduction (i.e., O₂ → O₂^{•-} → H₂O₂) or (ii) a one-step, two-electron reduction (i.e., O₂ → H₂O₂) [*Angew. Chem. Int. Ed.* **59**, 17356-17376 (2020)]. When we supplemented *p*-BQ to O₂-rich electrolyte solution, both AQC/CFP and CFP cathodes did not produce H₂O₂. This result indicates that the two-step, single-electron reduction is the sole pathway of electrocatalytic reduction of O₂ to H₂O₂.



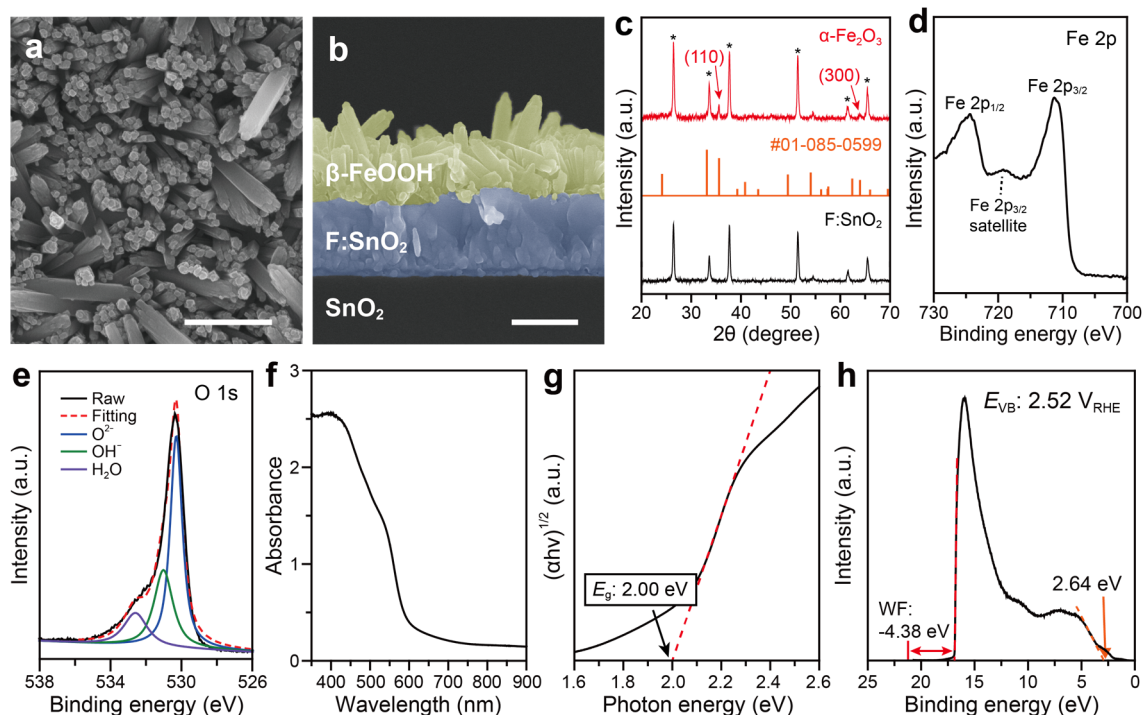
Supplementary Figure 5. Investigation of direct reduction of NAD⁺. Linear sweep voltammograms of carbon paper. Electrolyte solution: NaPi buffer (100 mM, pH 7.5). NAD⁺ concentration: 1 mM. Geometrical surface area of cathode: 1 cm². Scan rate: 25 mV s⁻¹.



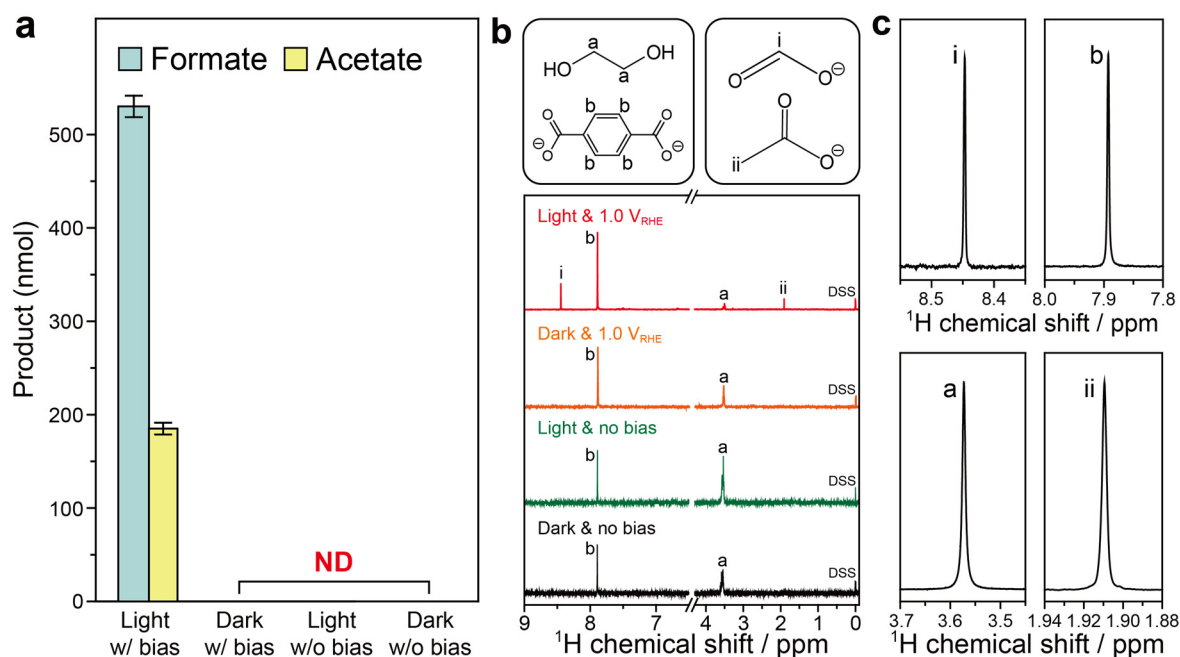
Supplementary Figure 6. Spectroscopic analysis for NADH regeneration. ^1H NMR spectra of NADH, NAD^+ , and M_{ox} . Solvent: a mixture of NaPi buffer (100 mM, pH 7.5) and D_2O (volume ratio: 9/1). In the M_{ox} 's NMR spectrum, the ratio of integration of the four assigned peaks was 1:1:1:1. We used DSS as a chemical shift standard.



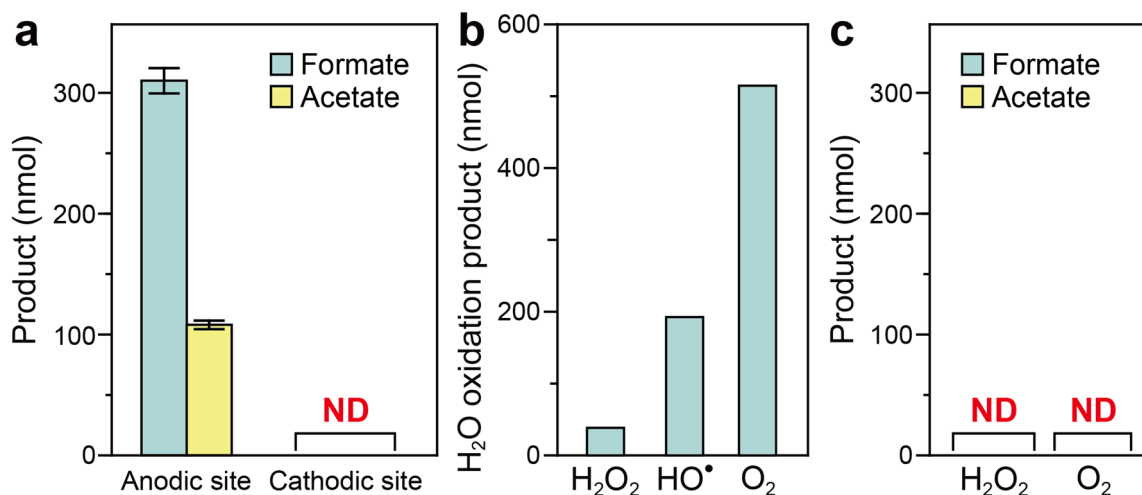
Supplementary Figure 7. EC regeneration of NADH in different solvents. Applied bias: $-0.2 V_{\text{RHE}}$. Concentration of NAD^+ : 1 mM. Concentration of M_{ox} : 0.25 mM. Working electrode: CFP cathode. Error bar: standard deviation ($n = 3$). NS: not significance.



Supplementary Figure 8. Characterization of β -FeOOH and α -Fe₂O₃. (a) Plan-view SEM image of β -FeOOH. (b) Cross-sectional SEM image of the β -FeOOH. Scale bar: 500 nm. (c) X-ray diffraction (XRD) pattern of α -Fe₂O₃ on F:SnO₂. The powder diffraction file number of α -Fe₂O₃ is #01-085-0599, which is provided by the joint committee on powder diffraction standards-international center for diffraction data (JCPDS-ICDD). Asterisks(*) indicate the XRD peaks of F:SnO₂. XPS spectra of α -Fe₂O₃ for (d) Fe 2p and (e) O 1s. The Fe 2p spectrum shows a Fe 2p_{1/2} and Fe 2p_{3/2}, respectively, which we attribute to Fe³⁺ state [*Adv. Healthcare Mater.* **6**, 1601133 (2017)]. The O 1s spectrum exhibits a major peak at ca. 530 eV, which corresponds to O²⁻ state in the Fe₂O₃ material. (f) Ultraviolet-visible spectrum of α -Fe₂O₃ film. (g) Tauc plot of α -Fe₂O₃ to estimate its indirect optical bandgap. (h) Ultraviolet photoelectron spectrum (UPS) of α -Fe₂O₃. Light source: helium lamp emitting at 21.2 eV (He I radiation). WF: work function. E_{VB} : valence band edge potential. As displayed in **Panels (a) and (b)**, the β -FeOOH film consisted of nanorods (diameter: 37 ± 5 nm, length: 297 ± 57 nm) roughly perpendicular to the F:SnO₂ substrate. After rinsing the β -FeOOH thin film with deionized water, we annealed it in air at 1,073 K to transform the crystal phase from β -FeOOH to α -Fe₂O₃; we confirmed the formation of α -Fe₂O₃ phase using XRD analysis [**Panel (c)**]. The thermal treatment also changed the square rod morphology to a worm-like structure (90 ± 12 nm in diameter, 312 ± 91 nm in length) with nanoporous network. Next, we carried out XPS on the as-synthesized α -Fe₂O₃ energy material, and confirmed that it contained Fe and O atoms in the Fe³⁺ and O²⁻ states, respectively, at the surface of α -Fe₂O₃ [**Panels (d) and (e)**].

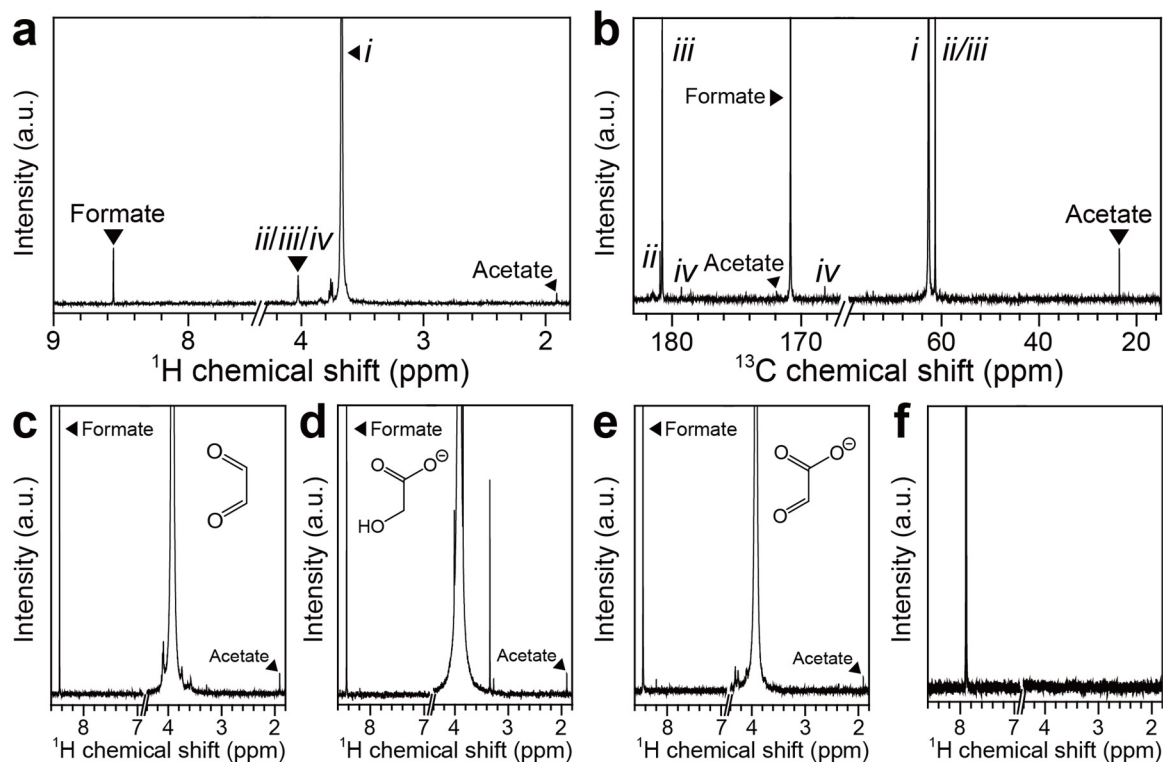


Supplementary Figure 9. A series of control experiments for photoanodic reactions using PET microplastics. (a) A series of control experiments for photoanodic transformation of PET at 1.0 V_{RHE}. We used quantitative ¹H NMR spectroscopy to quantify oxidation products. (b) ¹H NMR spectra of positive and control groups for PEC reformation of PET. We used maleic acid and DSS as a quantification standard and a chemical shift standard, respectively. Top: molecular structures of polymer components and oxidation products. (c) ¹H NMR spectra of pure samples of the oxidation products and polymer components in a mixture of 5 M NaOH aqueous solution and D₂O (volume ratio: 9/1). The chemical shift was calibrated using DSS. Photoelectrode used in (a, b): 1.7-cm² α-Fe₂O₃. Light source in (a, b): solar simulator (AM 1.5G, 100 mW cm⁻²). Electrolyte solution used in (a, b): unpretreated PET solution (1 mg mL⁻¹ PET microplastics, 5 M NaOH). Temperature in (a, b): 303 K. Reaction time in (a, b): 12 h. ND: not detected.

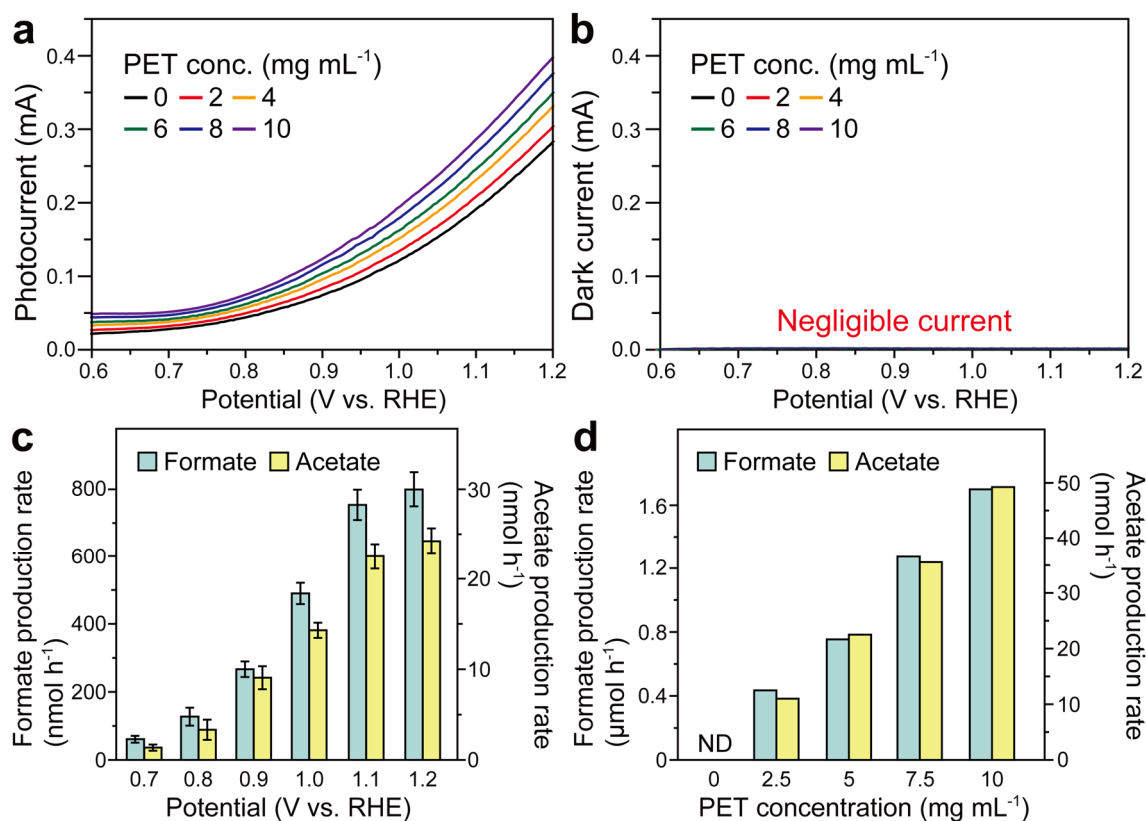


Supplementary Figure 10. Mechanistic studies of α -Fe₂O₃-driven photoanodic reactions.

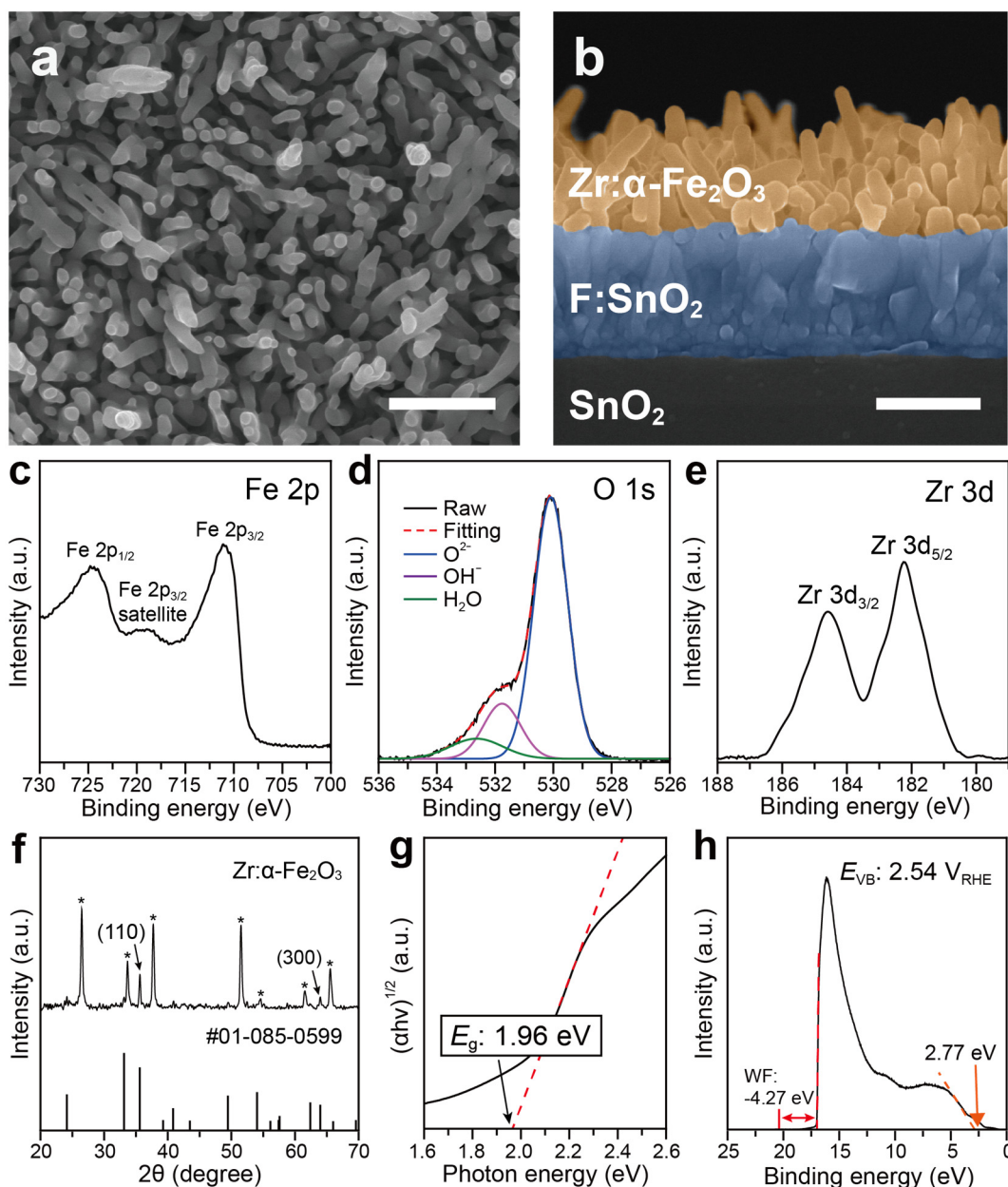
(a) Production of formate and acetate at anodic and cathodic sites for 12-h PEC reaction. We separated photoanodic and cathodic sites. Anolyte and catholyte: unpretreated PET solution (1 mg mL⁻¹ PET microplastics, 5 M NaOH). (b) α -Fe₂O₃-driven water oxidation reactions in 5 M NaOH for 1 h. We detected H₂O₂ and HO[•] using ABTS/HRP and coumarin assays, respectively. We measured O₂ gas using a head-space gas chromatograph. (c) Imperceptible production of formate and acetate after addition of H₂O₂ molecules or purging of O₂ gas into unpretreated PET solution (1 mg mL⁻¹ PET microplastics, 5 M NaOH) under dark conditions. Incubation time: 24 h. Concentration of H₂O₂: 100 mM. Temperature in (a-c): 303 K. Light condition in (a) and (b): 1 sun. Applied bias in (a) and (b): 1.0 V_{RHE}. ND: not detected.



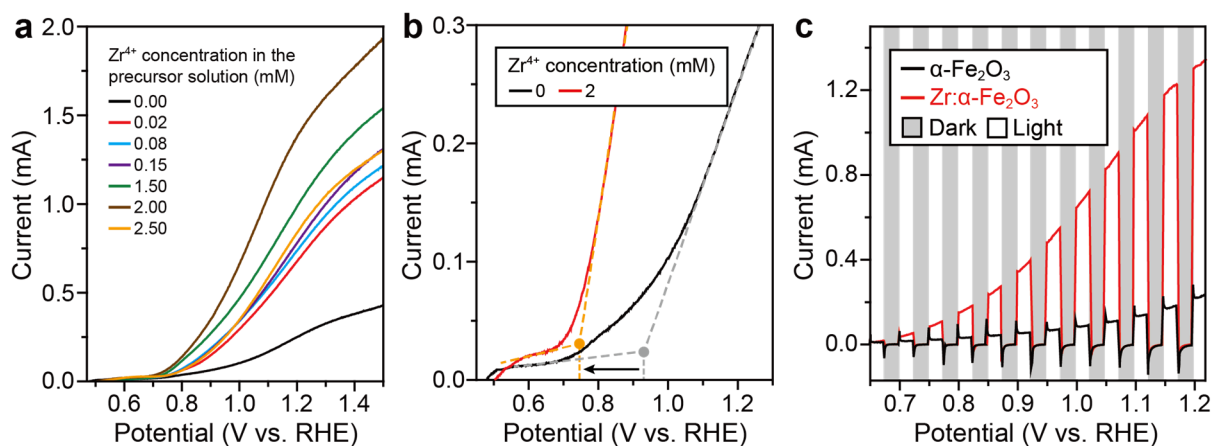
Supplementary Figure 11. PEC oxidation reactions of PET components and intermediates driven by α -Fe₂O₃ photoelectrode. (a) ¹H NMR and (b) ¹³C NMR spectra of 500 mM ethylene glycol (EG) after photoanodic reactions (1 sun, 1.0 V_{RHE}, 303 K, 5 M NaOH, 24 h). When we prepared ¹³C NMR samples, we repeated the PEC reactions 10 times, collected respective reaction solutions, and lyophilized the solutions to increase the concentrations of oxidation products. Labels: (i) EG, (ii) glyoxal, (iii) glycolate, and (iv) glyoxylate. ¹H NMR spectra of (c) 300 mM glyoxal, (d) 300 mM glycolate, (e) 300 mM glyoxylate, and (f) 1 mM benzene-1,4-dicarboxylate (BD) after PEC reactions (AM 1.5G, 100 mW cm⁻², 1.0 V_{RHE}, 303 K, 5 M NaOH, 3 h). Because of low aqueous solubility of BD, we could not dissolve a high concentration of BD. PEC reactions in highly alkaline solutions can drive various reactions, which accounts for the formation of unidentified oxidation products [*J. Am. Chem. Soc.* **141**, 15201-15210 (2019)].



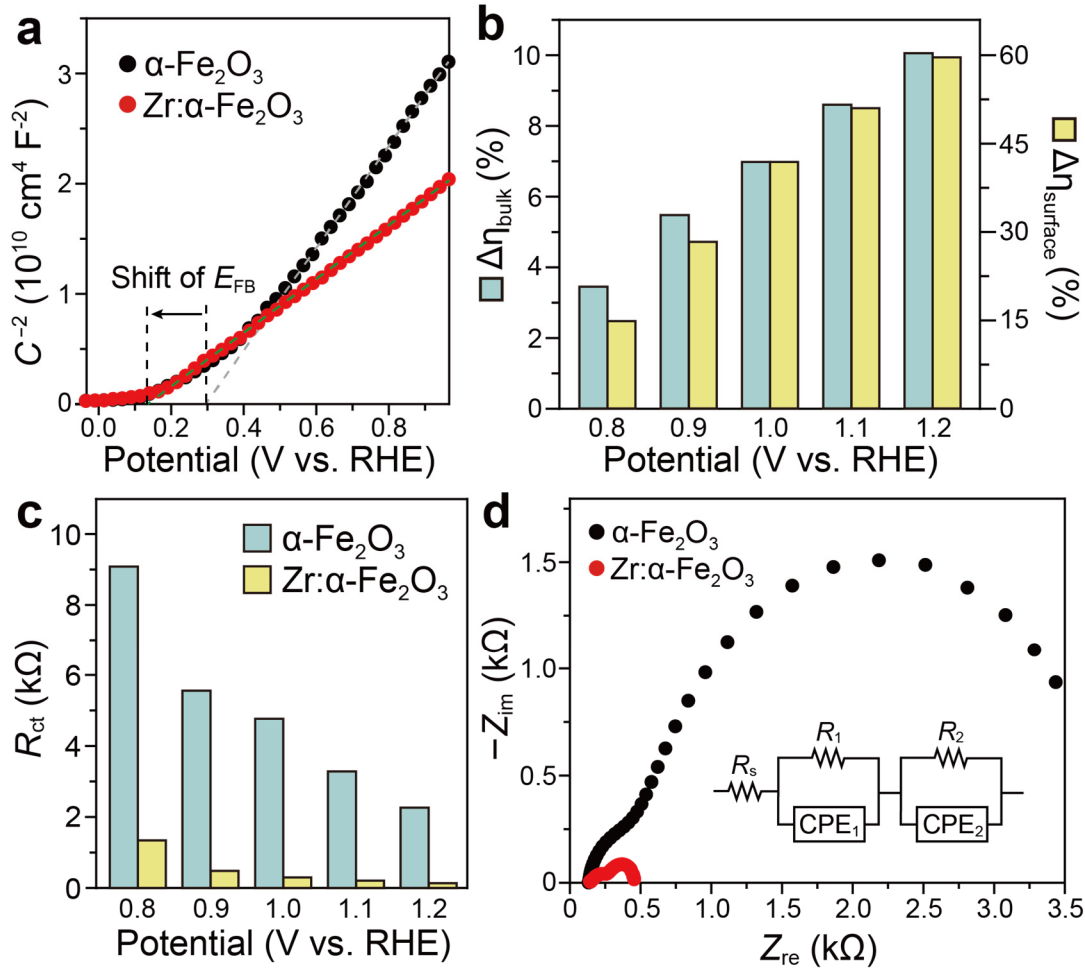
Supplementary Figure 12. Effect of applied bias and PET concentration on PEC reformation of PET microplastics. Linear sweep voltammograms of α -Fe₂O₃ with various concentrations of PET under (a) light or (b) dark conditions. Scan rate: 50 mV s⁻¹. Influence of (c) applied bias and (d) PET concentration on formation rates of oxidation products. Photoelectrode used in (a-d): 1.7-cm² α -Fe₂O₃. Light source used in (a, c, d): solar simulator (AM 1.5G, 100 mW cm⁻²). Electrolyte solutions: (a, b, d) pretreated PET solution (a specific concentration of PET microplastics, 5 M NaOH), and (c) pretreated PET solution (5 mg mL⁻¹ PET microplastics, 2 mL, 5 M NaOH). Applied bias in (d): 1.1 V_{RHE}. Temperature: 303 K. ND: not detected. The measurement was performed in triplicate, and all reported values represent means \pm standard deviation. We attribute the kinetic results [panels (c) and (d)] to an increase in (i) free holes' concentration at the α -Fe₂O₃|electrolyte interface (by enhancing applied bias) and (ii) substrates' density of electrical states (by increasing PET concentration); these two factors dominate the rates of photoinduced charge transfer according to the Gerischer's theory [*Chem. Soc. Rev.* **46**, 4645-4660 (2017)].



Supplementary Figure 13. Characterization of Zr: α -Fe₂O₃ electrode synthesized using 2 mM Zr⁴⁺ ions. (a) Plan-view SEM image of Zr: α -Fe₂O₃ film. Scale bar: 500 nm. (b) Cross-sectional SEM image of the photoelectrode. Scale bar: 500 nm. XPS spectra of Zr: α -Fe₂O₃ for (c) Fe 2p, (d) O 1s, and (e) Zr 3d. (f) XRD pattern of Zr: α -Fe₂O₃. The powder diffraction file number of hematite phase is #01-085-0599, which JCPDS-ICDD provides. Asterisks denote the XRD peaks of F:SnO₂. (g) Tauc plot of Zr: α -Fe₂O₃ to estimate its indirect bandgap. (h) UPS of Zr-doped α -Fe₂O₃. Compared with α -Fe₂O₃, Zr: α -Fe₂O₃ exhibited very similar morphology (worm-like structure), hematite phase, optical bandgap (1.96 eV), valence band edge potential (2.54 V_{RHE}), and conduction band edge potential (0.58 V_{RHE}). Note that the Zr 3d XPS spectrum displays two clear peaks at approximately 182.2 and 184.5 eV, indicating the Zr⁴⁺ oxidation state [*Nanoscale* **5** 9867-9874 (2013)]. In addition, the chemical states of Fe and O atoms were Fe³⁺ and O²⁻ according to their XPS peak positions.



Supplementary Figure 14. Effect of Zr doping on PEC performance of hematite-based photoanodes. (a) Dependency of Zr concentrations on Zr: α -Fe₂O₃'s photocurrent. (b) Shift of onset potentials of H₂O oxidation caused by Zr doping on α -Fe₂O₃. We determined the onset potentials by (i) linearly extrapolating the rapidly rising portion of the anodic wave and the baseline portion of the current and (ii) estimating the intersection of the extrapolated lines. The concentrations of Zr⁴⁺ in a precursor solution are shown at the upper left corner of (a) and (b). Higher concentrations of Zr⁴⁺ decreased the photoanodic current, which is attributed to an overly narrow depletion region and a consequent reduced charge separation efficiency [*Solar RRL* **4**, 1900509 (2020)]. (c) Chopped linear sweep voltammograms of α -Fe₂O₃ and Zr: α -Fe₂O₃ photoanodes. The Zr: α -Fe₂O₃ was synthesized using 2 mM Zr⁴⁺ in a precursor solution. Scan rate: 5 mV s⁻¹. Geometrical surface area of photoanodes in (a-c): 1.7 cm². Electrolyte solution in (a-c): aqueous 5 M NaOH. Light intensity in (a-c): 1 sun. Temperature in (a-c): 303 K.

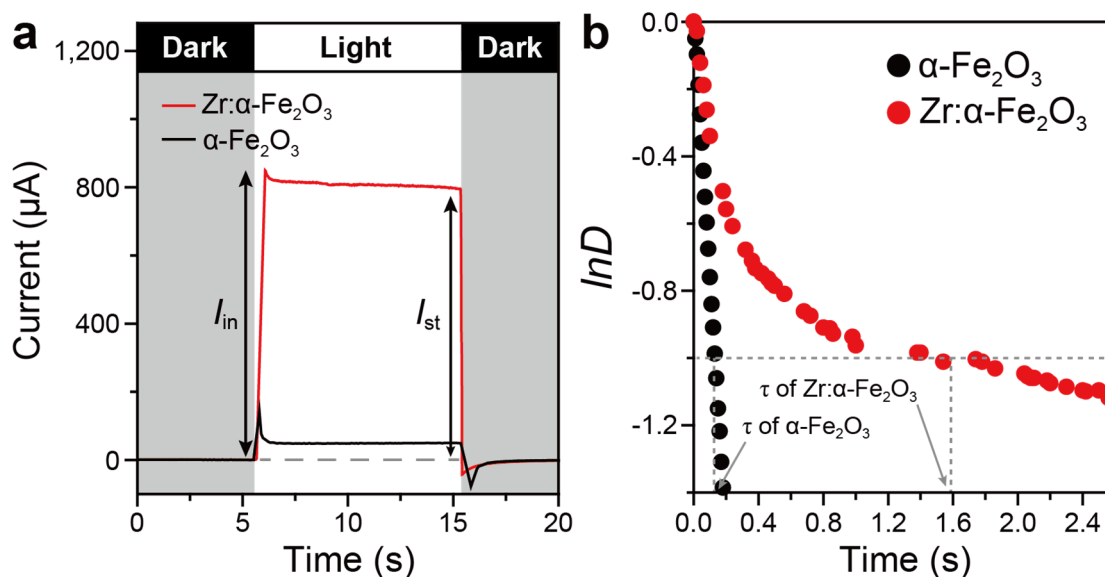


Supplementary Figure 15. Comparison of PEC properties of hematite-based photoanodes. (a) Mott-Schottky plots. Frequency: 1 kHz. E_{FB} : flat-band potential. A positive slope in a Mott-Schottky plot is a characteristic of n-type semiconductors. (b) Comparison of charge separation efficiencies in the bulk (η_{bulk}) and at the surface ($\eta_{surface}$) of $\alpha\text{-Fe}_2\text{O}_3$ -based photoanodes. $\Delta\eta \equiv \eta$ of $\text{Zr}:\alpha\text{-Fe}_2\text{O}_3 - \eta$ of $\alpha\text{-Fe}_2\text{O}_3$. $\eta_{bulk} = J_{SO_3} \times J_{abs}^{-1}$. $\eta_{surface} = J_{PET} \times J_{SO_3}^{-1}$. J_{SO_3} is the photocurrent density for sulfite oxidation, J_{PET} is the photocurrent density for PET oxidation, and J_{abs} is the rate of photon absorption expressed as current density. Electrolyte solution: pretreated PET solution (5 mg mL⁻¹ PET microplastics, 5 M NaOH) or 5 M NaOH solution containing 300 mM Na₂SO₃. Light source: solar simulator (AM 1.5G, 100 mW cm⁻²). (c) Charge-transfer resistances at different potentials. We estimated charge-transfer resistances by fitting their Nyquist plots to an equivalent circuit model, which consists of a series resistance, two charge-transfer resistances, and two constant phase elements. (d) Nyquist plots of $\alpha\text{-Fe}_2\text{O}_3$ and $\text{Zr}:\alpha\text{-Fe}_2\text{O}_3$ under solar light (1 sun) at 1.1 V_{RHE}. Frequency range: 100,000 to 0.1 Hz. Z_{re} and Z_{im} indicate real and imaginary impedance, respectively. R_s : series resistance at the interface between F:SnO₂ substrate and hematite layer. R_1 : charge transport resistance in the bulk. CPE₁: constant phase element in the bulk of hematite. R_2 : charge-transfer resistance at the hematite|electrolyte interface. CPE₂: constant phase element of the interface. The inset is an equivalent circuit model to estimate charge transfer resistances of the photoanodes.

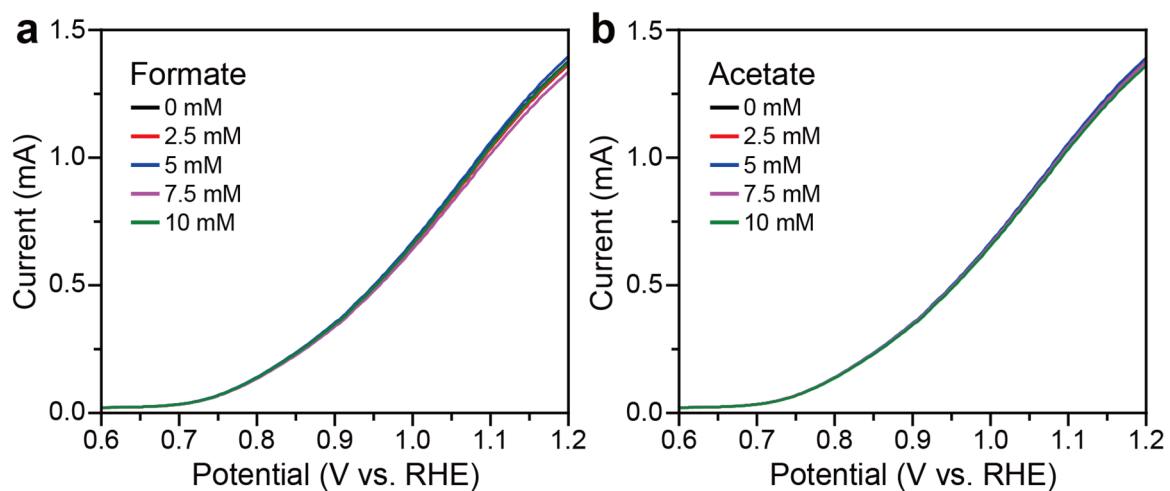
We confirmed the rise in the majority carrier concentration using electrochemical impedance spectroscopy (EIS) under dark conditions; our Mott-Schottky plots show that the carrier density of Zr: α -Fe₂O₃ is higher ($2.43 \times 10^{20} \text{ cm}^{-3}$) than that of α -Fe₂O₃ ($1.24 \times 10^{20} \text{ cm}^{-3}$) [**Panel (a)**]. Furthermore, Zr doping resulted in improved charge separation efficiencies in the bulk (η_{bulk}) and at the surface (η_{surface}) (see detailed calculation procedures in the Methods section). As shown in **Panel (b)**, Zr: α -Fe₂O₃ exhibited higher η_{bulk} and η_{surface} from 0.8 to 1.2 V_{RHE}. We attribute it to the increase in electron concentration and electrical conductivity; α -Fe₂O₃'s poor majority carrier conductivity is reported to result in a low charge separation efficiency [*J. Mater. Chem. A* **3**, 16896-16912 (2015)].

We further verified better charge transport properties of Zr: α -Fe₂O₃ by obtaining Nyquist plots from EIS under solar light at various applied bias. As shown in **Panel (c)**, the charge-transfer resistances of Zr: α -Fe₂O₃ were lower than those of α -Fe₂O₃ from 0.8 to 1.2 V_{RHE}. It indicates Zr: α -Fe₂O₃'s enhanced charge mobility and reduced charge recombination caused by its increased carrier density. A characteristic Nyquist plot of each photoanode is shown in **Panel (d)**.

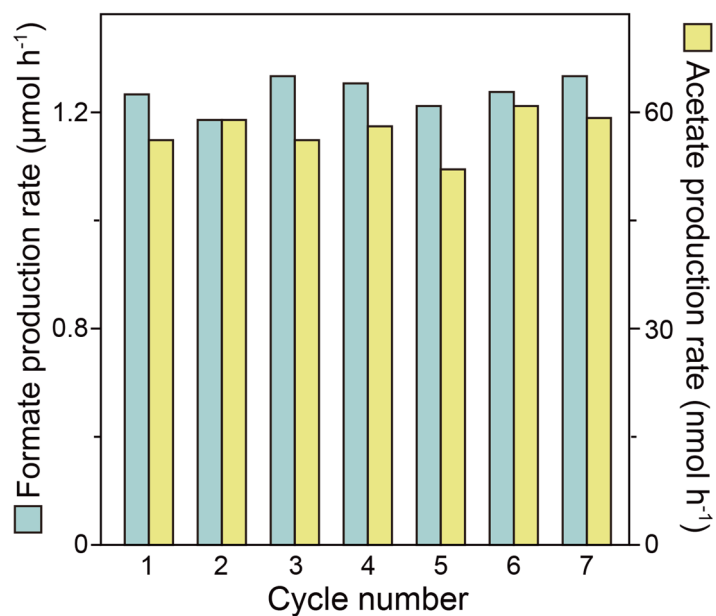
On the other hand, Zr doping gave rise to a lowered the flat-band potential. The Mott-Schottky plots display a cathodic shift of flat-band potential by 0.16 V [**Panel (a)**], which accounts for the cathodic shift of onset potential of Zr: α -Fe₂O₃ (**Supplementary Fig. 14b**). The lowered flat-band potential indicates an upward band bending for faster photoelectrocatalytic reactions.



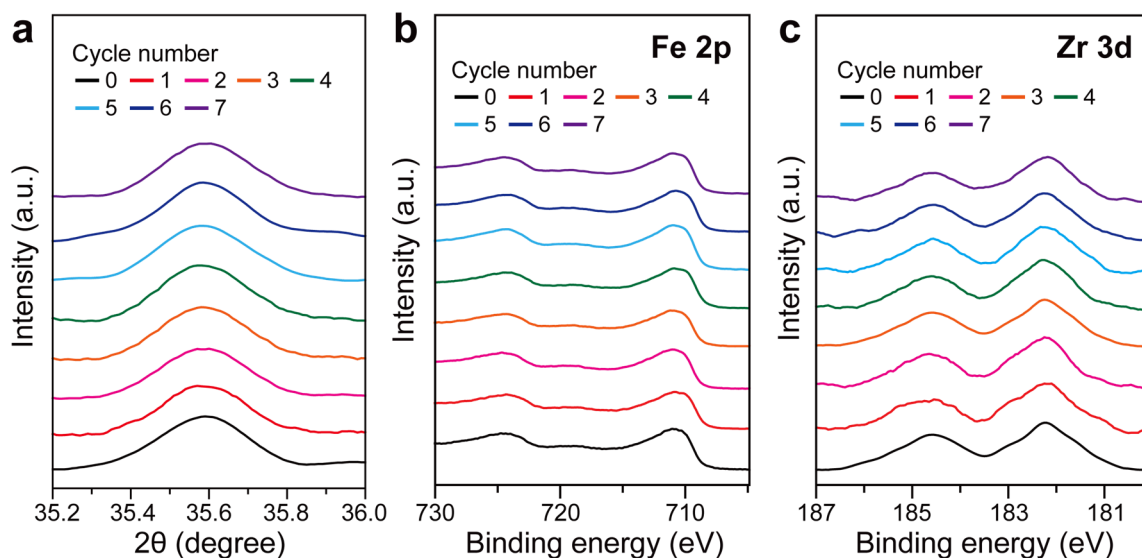
Supplementary Figure 16. Analysis of charge recombination behaviors of hematite-based photoanodes. (a) Transient photocurrent curves of $\alpha\text{-Fe}_2\text{O}_3$ and $\text{Zr}:\alpha\text{-Fe}_2\text{O}_3$ photoanodes at 1.0 V_{RHE} . I_{in} and I_{st} are initial and steady-state photocurrent, respectively. Note that positive photocurrent spikes originate from charge recombination until the photoanode reaches a quasi-equilibrium state, whereas negative spikes result from recombination of the photoexcited holes with free electrons. (b) Anodic transient dynamics of $\alpha\text{-Fe}_2\text{O}_3$ and $\text{Zr}:\alpha\text{-Fe}_2\text{O}_3$ under solar light. A normalized parameter (D) is defined as $D = (I_t - I_{\text{st}}) \times (I_{\text{in}} - I_{\text{st}})^{-1}$ where I_t is the time-dependent photocurrent in the **panel (a)** [*Nat. Commun.* **4**, 2651 (2013)]. The transient time constant (τ) is defined as the time when $\ln D = -1$, and reflects the general behavior of charge recombination and life-time of the charge carriers. We obtained additional evidence of $\text{Zr}:\alpha\text{-Fe}_2\text{O}_3$'s suppressed charge recombination using transient photocurrent measurements. **Panel (a)** shows that $\text{Zr}:\alpha\text{-Fe}_2\text{O}_3$'s positive and negative spikes were smaller than those of $\alpha\text{-Fe}_2\text{O}_3$. In addition, the transient time constant of $\text{Zr}:\alpha\text{-Fe}_2\text{O}_3$ was estimated to be 1.59 s, which was much longer than that of $\alpha\text{-Fe}_2\text{O}_3$ (0.12 s) [**Panel (b)**].



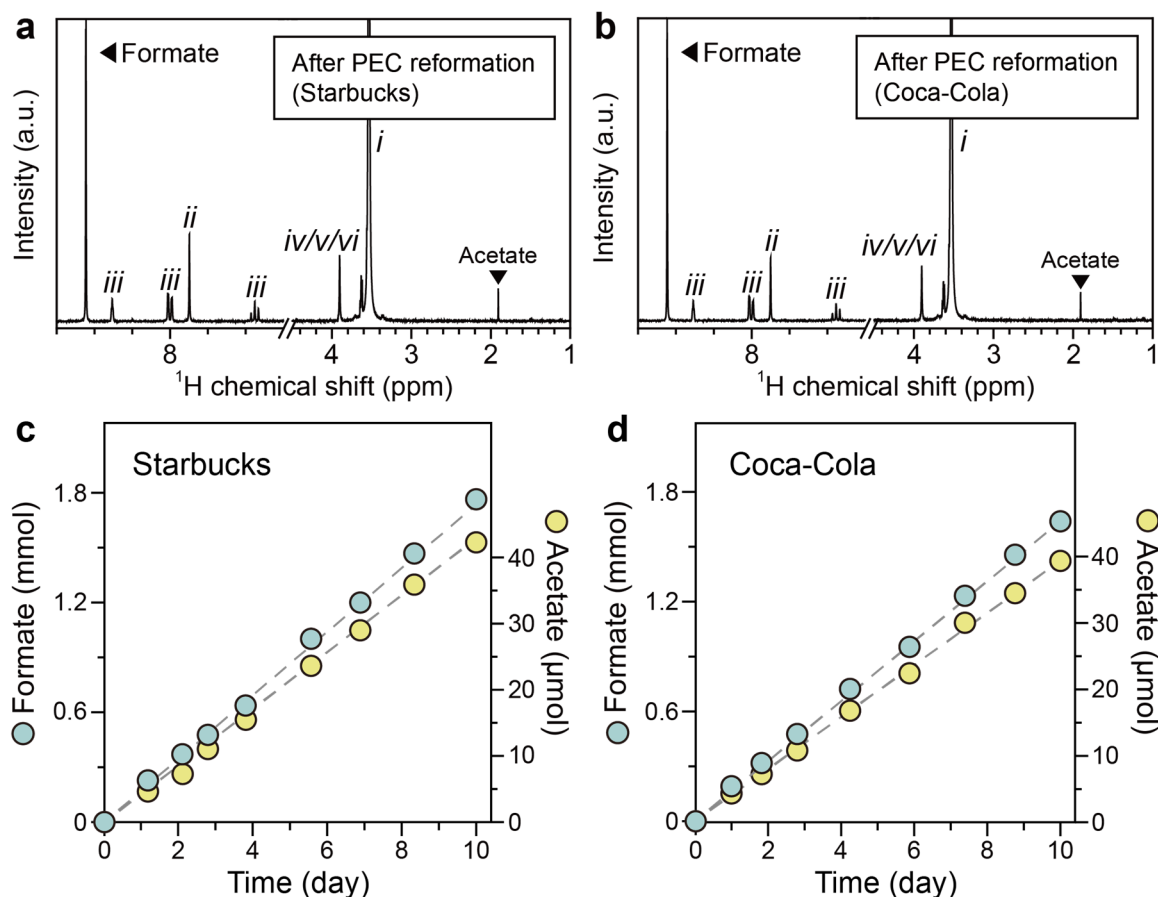
Supplementary Figure 17. Voltammetric analysis of Zr:α-Fe₂O₃ in the presence of formate or acetate. Linear sweep voltammograms of Zr:α-Fe₂O₃ in the presence of (a) formate or (b) acetate. Reaction condition: 1.7-cm² Zr:α-Fe₂O₃, formate or acetate, 5 M NaOH, simulated solar light (1 sun), and 303 K. Scan rate: 50 mV s⁻¹.



Supplementary Figure 18. Iteration test of Zr:α-Fe₂O₃-driven transformation of PET. Reaction condition: 1.7-cm² Zr:α-Fe₂O₃, pretreated PET solution (5 mg mL⁻¹ PET microplastics, 5 M NaOH), simulated solar light (AM 1.5G, 100 mW cm⁻²), 1.1 V_{RHE}, and 303 K.

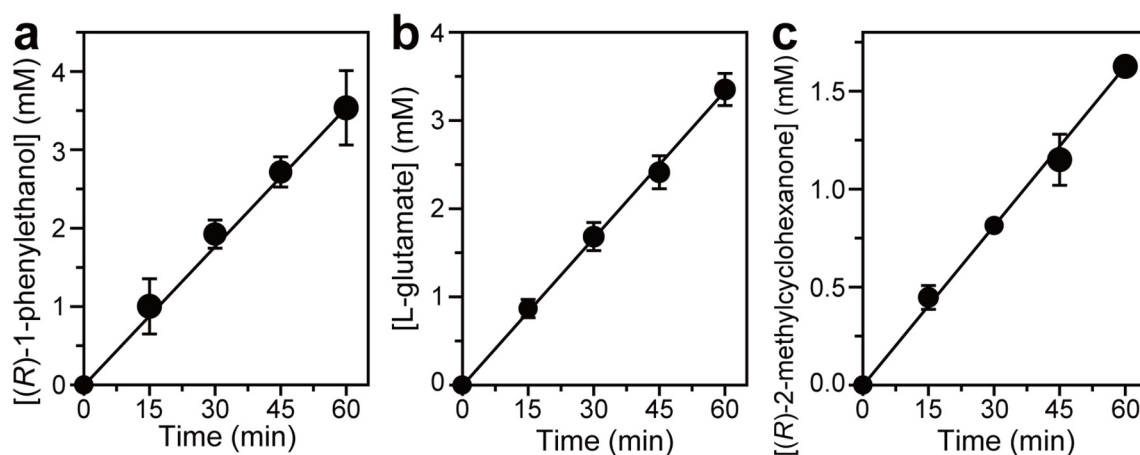


Supplementary Figure 19. Changes in phase and chemical states of Zr:α-Fe₂O₃ photoanode after PEC reformation reactions. Changes in (a) XRD patterns, (b) Fe 2p XPS spectra, and (c) Zr 3d XPS spectra of Zr:α-Fe₂O₃ electrode after the PEC iteration test. Working electrode: 1.7-cm² Zr:α-Fe₂O₃. Electrolyte solution: pretreated PET solution (5 mg mL⁻¹ PET microplastics, 5 M NaOH). Light source: xenon lamp (AM 1.5G, 100 mW cm⁻²), Applied bias: 1.1 V_{RHE}. Temperature: 303 K.

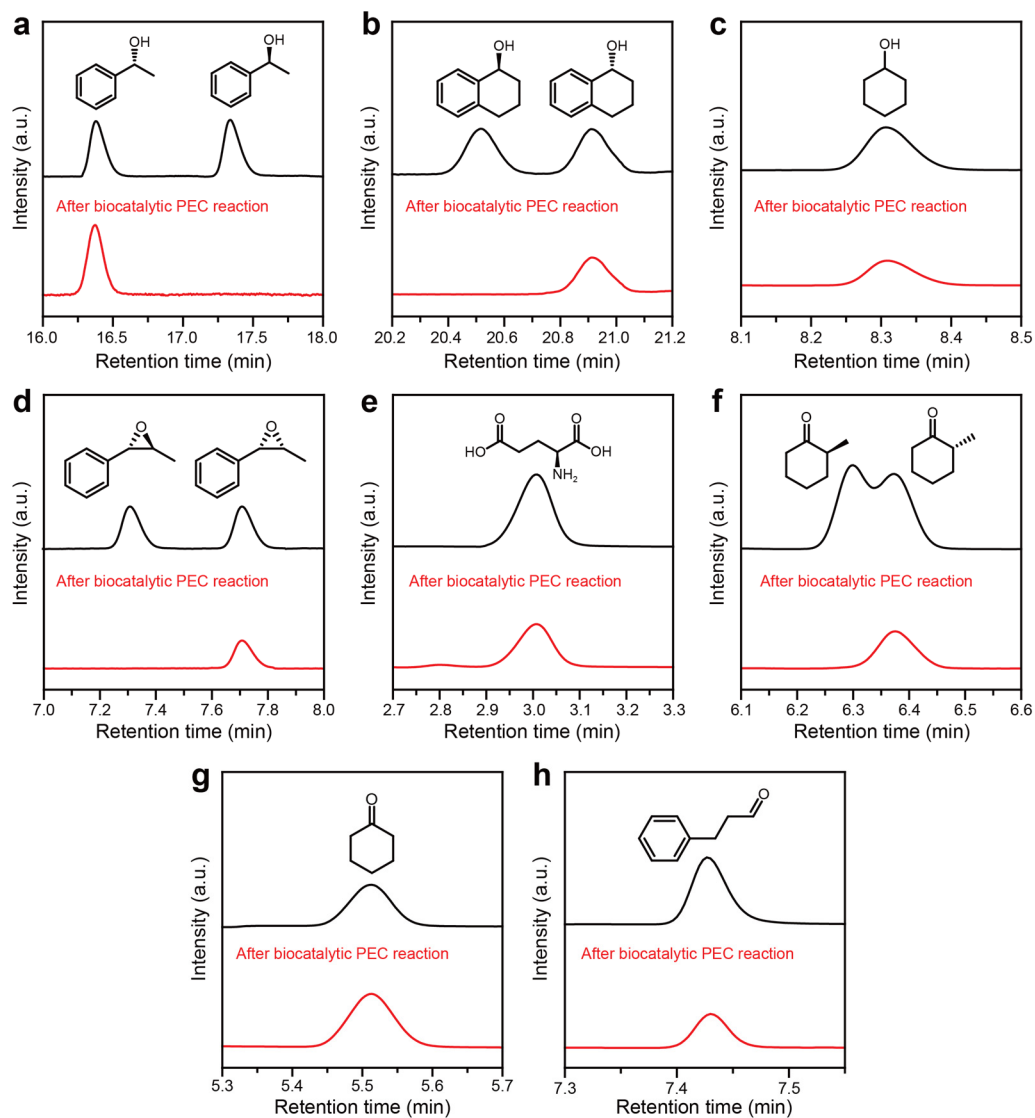


Supplementary Figure 20. Zr: α -Fe $_2$ O $_3$'s PEC reformation of post-consumer PET items.

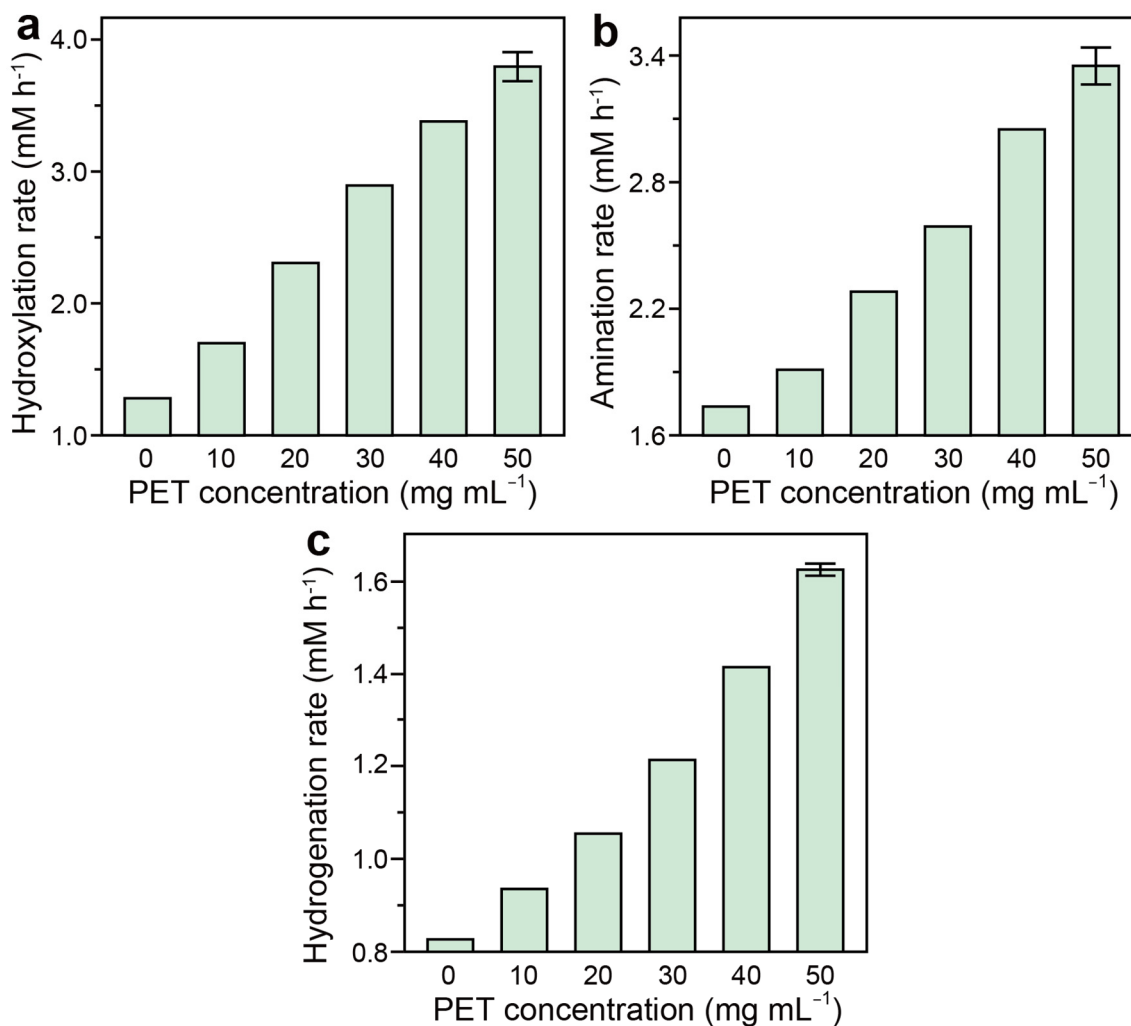
PET is a commonly used polymer in consumables in the beverage industry. Representative examples include a Starbucks cup and a Coca-Cola bottle. ^1H NMR spectra of PET microplastics from (a) Starbucks and (b) Coca-Cola companies after PEC reactions. Labels: (i) EG, (ii) BD, (iii) isophthalate, (iv) glyoxal, (v) glycolate, and (vi) glyoxylate. Isophthalate, an isomer of BD, can be used in the synthesis of commercial PET merchandise. Time profiles of production of formate and acetate through PEC transformation of nonrecyclable PET microplastics obtained from (c) Starbucks PET disposable cup and (d) Coca-Cola PET bottle. Reaction condition in (a-d): unpretreated PET solution (50 mg mL $^{-1}$ PET microplastics, 5 M NaOH, 80 mL), simulated solar light (AM 1.5G, 100 mW cm $^{-2}$, 10 days), 1.1 V $_{\text{RHE}}$, and 303 K.



Supplementary Figure 21. Controlled potential photoelectrolysis for enzymatic reactions. List of enzymatic products: (a) (*R*)-1-phenylethanol, (b) L-glutamate, and (c) (*R*)-2-methylcyclohexanone. Anodic electrolyte: pretreated PET solution (PET microplastics, 5 M NaOH) using post-consumer Starbucks PET disposable cups. Cathodic electrolyte in (a): 50 nM *rAaeUPO* and 16 mM ethylbenzene in an O₂-rich KPi buffer (100 mM, pH 6.0). Cathodic electrolyte in (b): 500 nM GDH, 80 mM α -ketoglutarate, 250 mM NH₄⁺, 0.25 mM **M**_{ox}, and 1 mM NAD⁺ in an O₂-depleted NaPi buffer (100 mM, pH 7.5). Cathodic electrolyte in (c): 5 μ M *TsOYE*, 7 mM 2-methyl-2-cyclohexen-1-one, 10 mM CaCl₂, 20 mM NH₄⁺, 0.25 mM **M**_{ox}, and 1 mM NAD⁺ in an O₂-depleted TEOA-buffered solution (100 mM, pH 7.5). Light condition: 1 sun (AM 1.5G, 100 mW cm⁻²). Applied bias: (a) 1.2 V, (b) 1.0 V, and (c) 1.0 V. Temperature: 303 K. The error bars correspond to the standard deviation ($n = 3$).

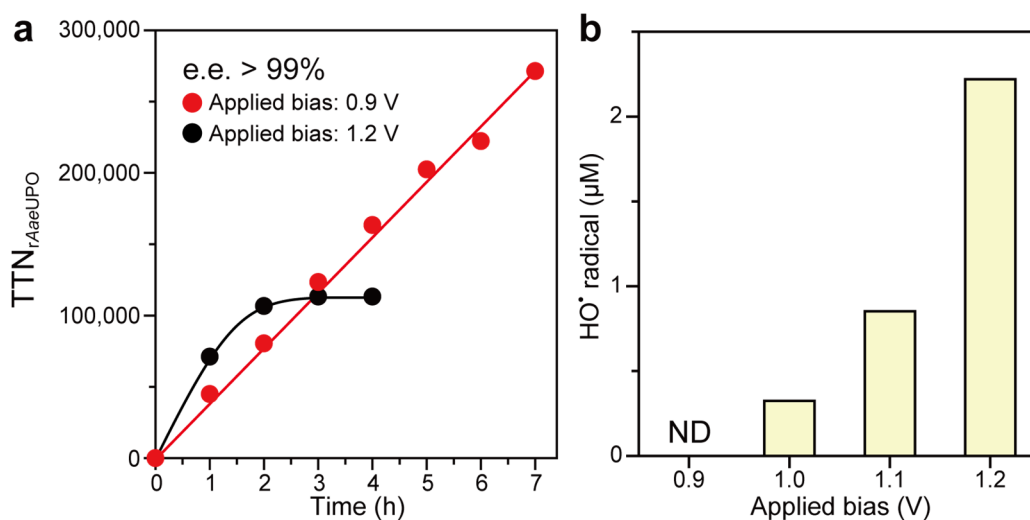


Supplementary Figure 22. Gas or liquid chromatograms of enzymatic products. (a) 1-Phenylethanol. **(b)** 1,2,3,4-Tetrahydro-1-naphthol. **(c)** Cyclohexanol. **(d)** 1-Phenylpropylene oxide. **(e)** L-glutamic acid. **(f)** 2-Methylcyclohexanone. **(g)** Cyclohexanone. **(h)** 3-Phenylpropionaldehyde.

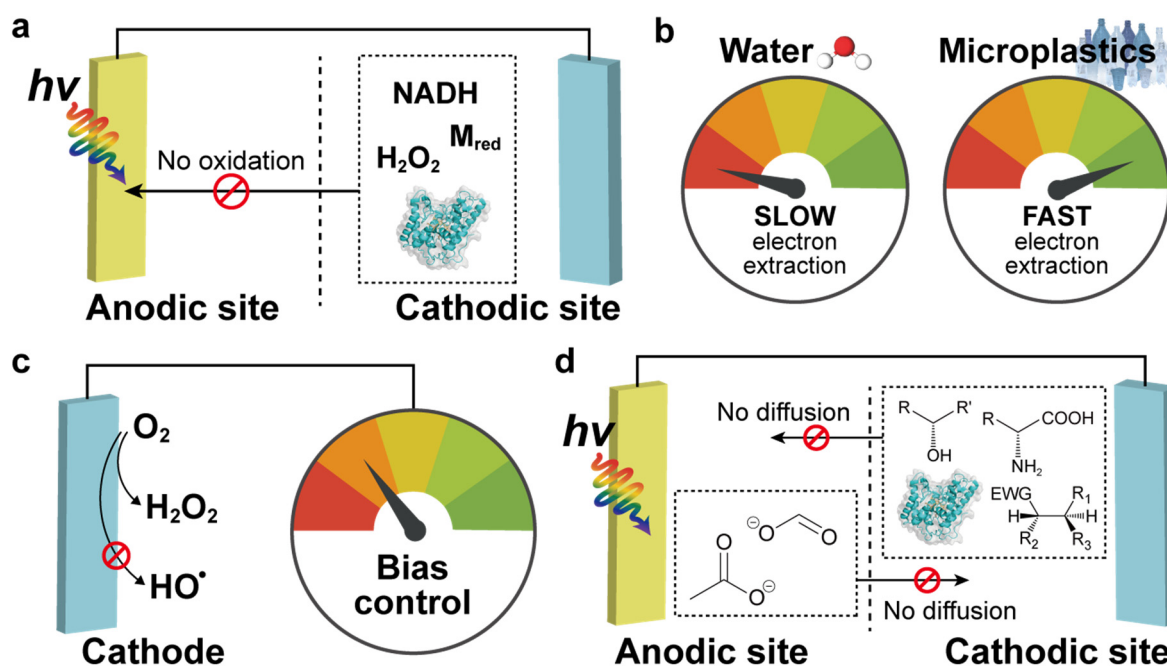


Supplementary Figure 23. Effect of PET concentration on the rates of BPEC reactions.

List of enzymatic reactions: **(a)** hydroxylation, **(b)** amination, and **(c)** hydrogenation. Anodic electrolyte: pretreated PET solution (PET microplastics, 5 M NaOH) using post-consumer PET disposable cups. Cathodic electrolyte in **(a)**: 50 nM *rAaeUPO* and 16 mM substrate in an O₂-rich KPi buffer (100 mM, pH 6.0). Cathodic electrolyte in **(b)**: 500 nM GDH, 80 mM α -ketoglutarate, 250 mM NH₄⁺, 0.25 mM M_{ox}, and 1 mM NAD⁺ in an O₂-depleted NaPi buffer (100 mM, pH 7.5). Cathodic electrolyte in **(c)**: 5 μ M *TsOYE*, 7 mM substrate, 10 mM CaCl₂, 20 mM NH₄⁺, 0.25 mM M_{ox}, and 1 mM NAD⁺ in an O₂-depleted TEOA-buffered solution (100 mM, pH 7.5). Light condition: 1 sun (AM 1.5G, 100 mW cm⁻²). Temperature: 303 K.



Supplementary Figure 24. Effect of applied bias on *rAaeUPO*-catalyzed hydroxylation reactions. (a) Time profiles of *rAaeUPO*'s total turnover number ($TTN_{rAaeUPO}$) at 0.9 and 1.2 V. Cathodic electrolyte: 50 nM *rAaeUPO* and 16 mM substrate in an O_2 -rich KPi buffer (100 mM, pH 6.0). (b) Formation of HO^\bullet at the cathodic site of $Zr:\alpha\text{-Fe}_2O_3|AQC/CFP$. Cathodic electrolyte: KPi buffer (100 mM, pH 6.0) containing 1 mM coumarin. Coumarin was used to detect the hydroxyl radicals. Anodic electrolyte in (a, b): pretreated PET solution (50 mg mL^{-1} PET microplastics, 5 M NaOH) using real-world PET disposable cups. Light intensity in (a, b): 1 sun. ND: not detected.



Supplementary Figure 25. PEC properties used to augment enzymatic performances. (a) Two-compartment fashion for protecting reduced mediators and redox enzymes from oxidation. (b) Flexible selection of anodic reactions, which can boost an electron extraction process for faster biocatalytic synthesis. (c) Bias control to drive redox reactions selectively. (d) Two-compartment configuration that separates oxidoreductases (and their products) from oxidation products. Because oxidation products are spatially separated from enzymes, the oxidation products cannot cause plausible detrimental effects on biocatalytic processes.